Restoration of locomotor function following stimulation of the A13 region in Parkinson's mouse models.

Linda H. Kim[1,2*], Adam P. Lognon[1,2*], Sandeep Sharma[1,3], Michelle A. Tran[3], Cecilia Badenhorst[1,3], Taylor Chomiak[1,4], Stephanie Tam[3], Claire McPherson[3], Todd E. Stang[1,2], Shane E. A. Eaton[1,3], Zelma H. T. Kiss[1,2,4], Patrick J. Whelan[#1,3]
*These authors contributed equally.

Affiliations: [1]Hotchkiss Brain Institute, University of Calgary, Calgary, AB, Canada, T2N4N1, [2]Department of Neuroscience, University of Calgary, Calgary, AB, Canada, T2N 4N1, [3]Faculty of Veterinary Medicine, University of Calgary, Calgary, AB, Canada, T2N4N1, [4]Department of Clinical Neurosciences, University of Calgary, Calgary, AB, Canada, T2N 4N1

[#] **Corresponding author**
Patrick J. Whelan
HMRB 168,
3330 Hospital Drive NW,
University of Calgary
Calgary, AB
T2N 4N1
Email: whelan@ucalgary.ca

Short Title: Zona incerta mediated recovery of PD function

Author Contributions: LHK and APL performed experiments and prepared figures. CB and MAT prepared and edited figures. PJW edited figures and procured funding for the experiments. LHK, APL, ZHTK and PJW conceived and designed the research and interpreted the results. SS and APL performed surgeries for lesions, optogenetic experiments and conducted behavioral experiments. LHK and SEAE optimized light-sheet imaging. MAT, CB, ST, and CM performed manual cell counting. TES performed analysis. TC performed analysis and prepared figures on gait analysis. LHK, APL, TC, ZHTK, and PJW drafted the manuscript. All authors reviewed and approved the final version of the manuscript.

Competing Interest Statement: None.

Keywords: Dopamine, Connectome, Parkinson's Disease, Motor.

ABSTRACT

Parkinson's disease (PD) is characterized by extensive motor and non-motor dysfunction, including gait disturbance, which is difficult to treat effectively. This study explores the therapeutic potential of targeting the A13 region, a heterogeneous region of the medial zona incerta (mZI) containing dopaminergic, GABAergic, and glutamatergic neurons that has shown relative preservation in PD models. The A13 is identified to project to the mesencephalic locomotor region (MLR), with a subpopulation of cells displaying activity correlating to movement speed, suggesting its role in locomotion. We show that photoactivation of this A13 region can alleviate bradykinesia and akinetic features, while increasing turning in a mouse model of PD. These effects combine disease-specific rescue of function with a possible gain of function. We identified areas of preservation and plasticity within the A13 region using whole-brain imaging. Our findings suggest a global remodeling of afferent and efferent projections of the A13 region, highlighting the zona incerta's role as a crucial hub for the rapid selection of motor function. The study unveils the significant pro-locomotor effects of the A13 region and suggests its promising potential as a therapeutic target for PD-related gait dysfunction.

SIGNIFICANCE STATEMENT

This work examines the function of the A13 region in locomotion, an area with direct connectivity to locomotor regions in the brainstem. A13 stimulation can restore locomotor function and improve bradykinesia in a PD mouse model.

INTRODUCTION

Parkinson's disease (PD) is a complex condition affecting many facets of motor and non-motor functions, including visual, olfactory, memory and executive functions (Cenci and Björklund, 2020). Due to the widespread pathology of PD, focusing on changes within a single pathway cannot account for all symptoms. Gait dysfunction is one of the hardest to treat; pharmacological, deep brain stimulation (DBS) and physical therapies lead to only partial improvements (Nonnekes et al., 2020, 2015). While the subthalamic nucleus (STN) and globus pallidus (GPi) are common DBS targets for PD, alternative targets such as pedunculopontine nucleus (PPN) and the zona incerta (ZI) have been proposed with mixed results in improving postural and/or gait dysfunction (Caire et al., 2013; Ferraye et al., 2010; Gut and Winn, 2015; Hamani et al., 2011; Moro et al., 2010; Nonnekes et al., 2015; Okun and Foote, 2010; Ossowska, 2020; Stefani et al., 2007; Thevathasan et al., 2018). Most DBS work targeting the ZI has centred on areas close to the STN (Ossowska, 2020); however a common gap is the relative lack of knowledge regarding its downstream anatomical and functional connectivity with motor centers. Recent work with photoactivation of subpopulations of PPN neurons in PD models shows promise for similar ZI-focused strategies (Masini and Kiehn, 2022). Indeed our recent work on preclinical models shows that DBS of the A13 in rat models effectively produces locomotor activity that can be incorporated into ongoing behavior (Bisht et al., 2025).

The ZI is recognized as an integrative hub, with roles in regulating sensory inflow, arousal, motor function, and conveying motivational states (Chometton et al., 2017; Mitrofanis, 2005; Monosov et al., 2022; Sharma et al., 2024; Wang et al., 2020; Yang et al., 2022; Zhao et al., 2019). As such, it is well placed to be involved in PD and has seen increased clinical and preclinical research over the last two decades (Blomstedt et al., 2018; Ossowska, 2020; Plaha et al., 2008). However, little attention has been placed on the medial zona incerta (mZI), particularly the A13, the only dopamine-containing region of the rostromedial ZI (Bolton et al., 2015; Kim et al., 2017; Sharma et al., 2018). Recent research in primates and mice (Peoples et al., 2012; Roostalu et al., 2019; Shaw et al., 2010) indicates that the A13 is preserved in 1-methyl-4-phenyl-1,2,3,6-tetrahydropyridine (MPTP)-based PD models. Yet it is not clear whether the A13 region substantially remodels in PD models as has been observed for other areas of the brain (Ji et al., 2023).

Recently, we discovered that the A13 located within the ZI projects to two areas of the mesencephalic locomotor region (MLR), the PPN and cuneiform nucleus (CUN) (Sharma et al., 2018), suggesting a role for A13 in locomotor function. Indeed, mini-endoscopic calcium recordings from calcium/calmodulin-dependent protein kinase IIα (CaMKIIα) populations in the rostral ZI, which includes the A13 nucleus, show a subpopulation of cells whose activity correlates with movement speed (Li et al., 2021). Since this region projects to the MLR, it is a potential motor pathway to target for gait improvement, which has been substantiated by our DBS work targeting the A13 in rats (Bisht et al., 2025). Photoactivation of glutamatergic MLR neurons alleviates motor deficits in mouse models that either transiently blocked dopamine transmission, or lesioned substantia nigra pars compacta (SNc) with 6-hydroxydopamine (6-OHDA) (Fougère et al., 2021; Masini and Kiehn, 2022). Phenomena such as kinesia paradoxa (Glickstein and Stein, 1991) in PD patients support the existence of preserved parallel motor pathways that can be engaged in particular circumstances to produce normal movement.

Additional support for parallel motor pathways in PD comes from studies showing functional changes in A13 (Hoffman et al., 1997; Périer et al., 2000). Nigrostriatal lesions affect cellular function and lead to anatomical remodeling in monoaminergic brain regions including widespread alterations in dopaminergic, noradrenergic, cholinergic, and serotoninergic neuronal populations, however global connectivity patterns from A13 have not been expored (Braak et al., 2003; Kish et al., 2008; Lim et al., 2009; Perez-Lloret and Barrantes, 2016; Roostalu et al., 2019; Scatton et al., 1983; Zweig et al., 1989). There is additional evidence showing parallel motor pathways in the A13. For example, the A13 connectome encompasses the cerebral cortex (Mitrofanis and Mikuletic, 1999), central nucleus of the amygdala (Eaton et al., 1994), thalamic paraventricular nucleus (Li et al., 2014), thalamic reuniens (Sita et al., 2007; Venkataraman et al., 2021), CUN and PPN (Sharma et al., 2018), superior colliculus (SC) (Bolton et al., 2015), and dorsolateral periaqueductal grey (PAG) (Messanvi et al., 2013; Sita et al., 2007), making the A13 an potential hub for goal-directed locomotion (Choi and McNally, 2017; Eaton et al., 1994; Messanvi et al., 2013; Mok and Mogenson, 1986; Moriya et al., 2020; Ogundele et al., 2017; Manjit K. Sanghera et al., 1991; M. K. Sanghera et al., 1991; Sita et al., 2007; Venkataraman et al., 2021).

Given the A13 region's role in gait control and its therapeutic potential in PD, we investigated the effects of its photoactivation in 6-OHDA mouse models. The targeted area includes the A13 and a portion of the medial zona incerta (mZI), collectively referred to as the A13 region throughout this study. Photoactivation of the A13 region alleviated bradykinetic and akinetic symptoms in a mouse model of unilateral nigrostriatal degeneration induced by 6-OHDA. Our exploratory work on input and output patterns in the A13 region in 6-OHDA mice, suggesting potential downstream targets mediating the effects of photoactivation. These findings demonstrate that the A13 region exerts strong pro-locomotor effects in both normal and PD mouse models. Portions of these data have been presented in abstract form. (Kim et al., 2021).

RESULTS

Unilateral 6-OHDA mouse model has robust motor deficits

The overall experimental design is illustrated in Figure 1A, along with a schematic in Figure 1B showing injections of 6-OHDA in the medial forebrain bundle (mFB) and AAVDJ-CaMKIIα-ChR2 virus into the mZI. We confirmed SNc degeneration in a well-validated unilateral 6-OHDA-mediated Parkinsonian mouse model (Thiele et al., 2012). The percentage of tyrosine hydroxylase (TH^+) cell loss normalized to the intra-animal contralesional side was quantified. 6-OHDA produced a significant lesion that decreased TH^+ neuronal SNc populations. As previously reported (Boix et al., 2015), the SNc ipsilesional to the 6-OHDA injection (n = 10) showed major ablation of the TH^+ neurons compared to sham animals (Figure 1C and D: n = 12).

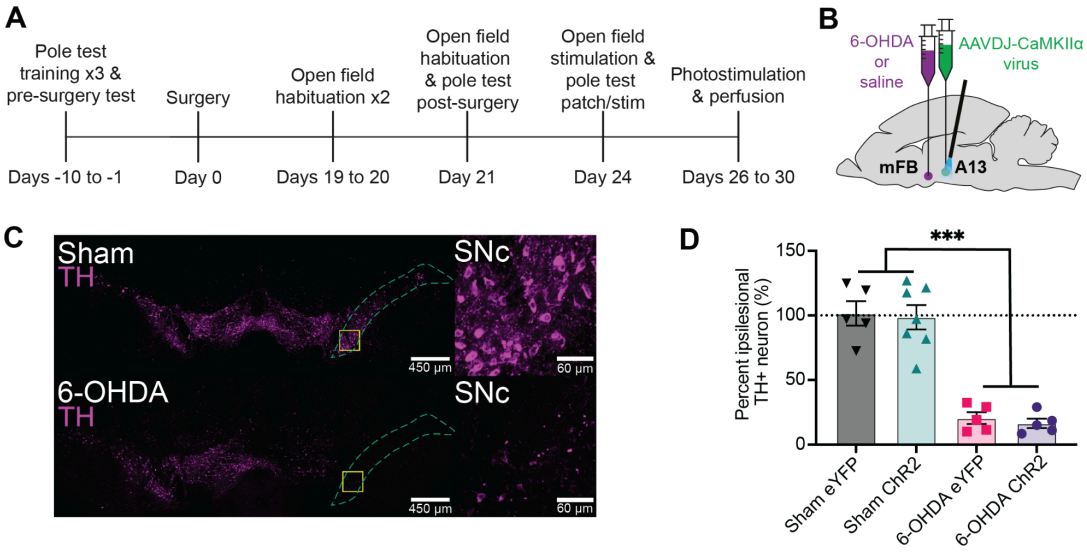

Figure 1. Experimental design and confirmation of unilateral TH⁺ depletion in the SNc via 6-OHDA lesion. (**A**) Illustration of experimental timeline. (**B**) Dual ipsilateral stereotaxic injection into the mFB and A13 region. (**C**) TH⁺ cells in the SNc of a sham animal (top) compared to a 6-OHDA–injected mouse (bottom). Magnified areas, outlined by yellow squares, are shown at right. (**D**) Unilateral injection of 6-OHDA into the mFB (6-OHDA ChR2: $n = 5$; 6-OHDA eYFP: $n = 5$) resulted in a significantly greater percentage loss of TH⁺ cells in the SNc compared to sham animals (sham ChR2: $n = 7$; sham eYFP: $n = 5$), regardless of virus type (two-way ANOVA: $F_{1,18} = 104.4$, $p < 0.001$). ***$p < 0.001$. Error bars indicate SEMs.

A13 region photoactivation generates pro-locomotor behaviors in the open field

6-OHDA lesions produce bradykinetic and akinetic phenotypes in the open field (Li et al., 2022; Magno et al., 2019; Sanders and Jaeger, 2016). We first confirmed localization of the optical fiber above the A13 region, centered on the mZI, along with YFP reporter expression in mice given sham or 6-OHDA injections (Figure 2; Figure 2 -figure supplement 1). Corroborating the *post hoc* targeting, we found evidence for c-Fos in neurons within the A13 region in photostimulated ChR2 mice (Figure 2D). We observed an increase in c-Fos fluorescence intensity in the A13 region of photostimulated 6-OHDA ChR2 mice compared to the 6-OHDA eYFP mice (Figure 2D-F). Before *post hoc* analysis, mice were monitored in the open field test (OFT), where the effects of the 6-OHDA lesion were apparent, with 6-OHDA lesioned animals demonstrating less movement, fewer bouts of locomotion, and less time engaging in locomotion (Figure 3A-E). Using instantaneous animal movement speeds that exceeded 2 cm/s as per Masini & Kiehn (2022), we plotted instantaneous speed (Figure 3B-E) and analyzed one-minute bins (Figure 3H). As was expected, 6-OHDA lesioned animals had lower movement speeds than sham control animals ($p < 0.001$). One animal from the 6-OHDA eYFP group was excluded because it did not meet the speed threshold during recording. Notably, photoactivation of the A13 region often generated dramatic effects, with mice showing a distinct increase in locomotor behavior (Figure 3A, Figure 3 - Video S1 & S2). Both sham and 6-OHDA ChR2 mice showed a significant increase in locomotor distance travelled during periods of photoactivation (Figure 3F, $p = 0.005$). One sham animal showed grooming behavior on stimulation and was excluded from the analysis.

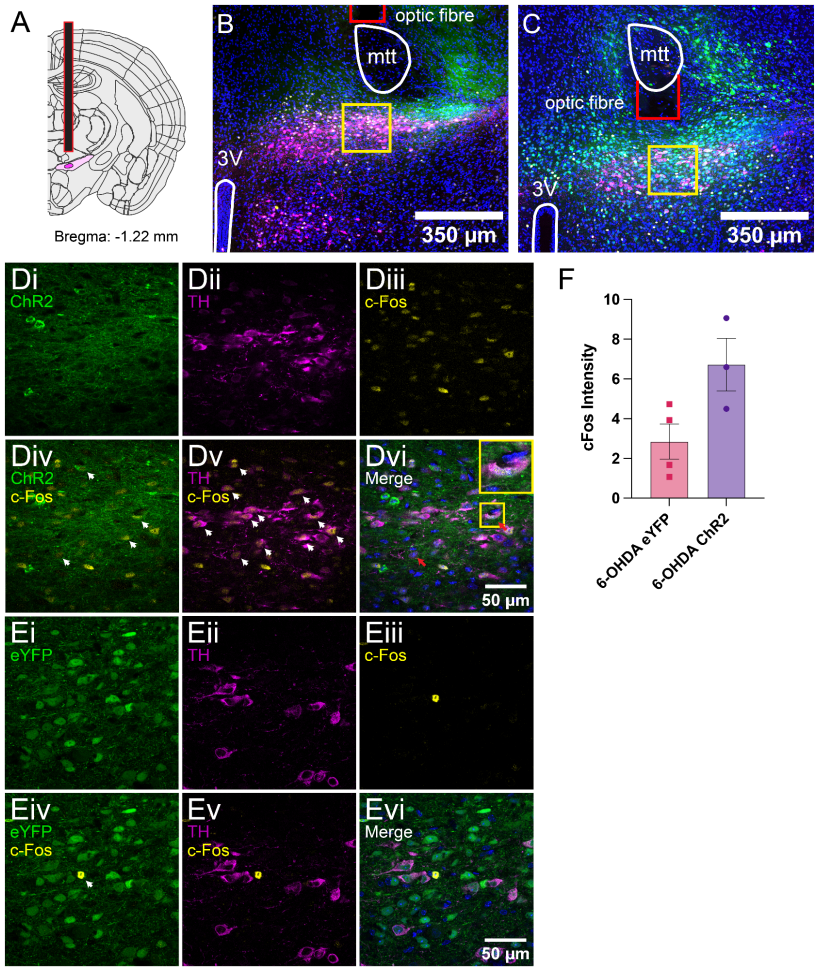

Figure 2. *Post hoc* c-Fos expression and targeting of the mZI and A13. (A) Diagram showing the A13 dopaminergic (DAergic) nucleus in dark magenta, encapsulated by the ZI in light magenta. The fiber-optic tip is outlined in red. Atlas image adapted from the Allen Brain Atlas (Goldowitz, 2010). **(B)** Tissue images were obtained from a 6-OHDA ChR2 animal and **(C)** a 6-OHDA eYFP animal. Images show the distribution of DAPI (blue), eYFP (green), c-Fos (yellow), and TH (magenta). Landmarks are outlined in white (3V: third ventricle; A13 and mZI as shown in A), and the optic cannula tip is shown in red. Higher-magnification images of the A13 DAergic nucleus are outlined by yellow boxes in a 6-OHDA ChR2 animal **(Di–Dvi)** and a 6-OHDA eYFP animal **(Ei–Evi)**. Images show isolated channels in the top rows of each group: **(i)** eYFP , **(ii)** TH , and **(iii)** c-Fos . Merged channels are shown in the bottom rows: **(iv)** eYFP/ChR2 + c-Fos, **(v)** TH + c-Fos, **(vi)** all three channels merged. White arrowheads in the merged images highlight areas of marker overlap. Red arrows indicate triple colocalization of ChR2, c-Fos, and TH. **(Dvi)** contains a magnified example of triple-labeled neurons, highlighted in the yellow box. **(F)** Graph shows an increase in c-Fos fluorescence intensity after photoactivation in 6-OHDA ChR2 mice ($p = 0.05$).

We tested whether photoactivation led to a single bout of locomotion or if there was an overall increase in bouts, signifying that animals could repeatedly initiate locomotion following photoactivation. Mice in the ChR2 groups demonstrated an increase in the number of locomotor bouts with photoactivation, indicating a greater ability to start locomotion from rest, and that photoactivation was not eliciting a single prolonged bout (Figure 3G, $p = 0.005$). Photoactivation also increased the total duration of locomotor bouts (Figure 3I, $p < 0.001$). We did note a refractory decrease in the distance travelled by the sham ChR2 group. To control for this, we compared the pre-stimulation timepoints to the baseline one-minute averages to ensure that the animal locomotion distance travelled returned to a stable state before stimulation was reapplied (Figure 3 – figure supplement 1, $p = 0.78$).

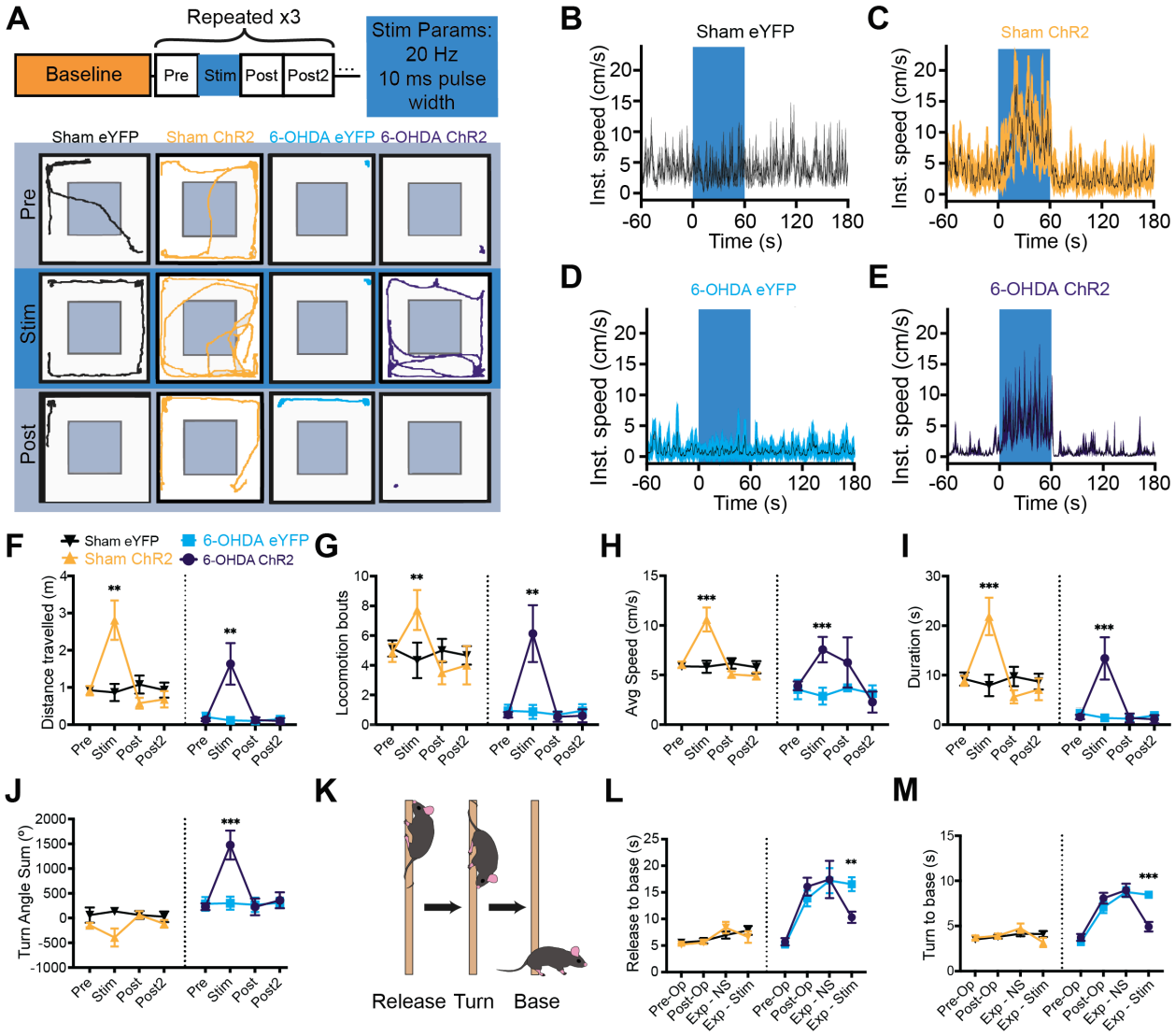

Figure 3. Ipsilesional photoactivation of the A13 region in a unilateral 6-OHDA mouse model rescues motor deficits.

(**A**) Schematic of the open-field experiment design and example traces from open-field testing. Each testing bin represents 1 min (total duration: 4 min) with unilateral photoactivation of the A13 region. (**B-E**) Group-averaged instantaneous velocity graphs showing no increase in a sham eYFP **(B)** or 6-OHDA eYFP mouse **(C)**, and increased velocity during stimulation in a sham ChR2 **(D)** and 6-OHDA ChR2 **(E)** mouse. (**F-I**) Effects of photoactivation on open-field metrics for sham eYFP (n = 5), sham ChR2 (n = 6), 6-OHDA eYFP (n = 5), and 6-OHDA ChR2 (n = 5) groups.Statistical comparisons used three-way mixed-model ANOVAs with post hoc Bonferroni pairwise tests. *Photoactivation significantly increased locomotor activity in both sham and 6-OHDA ChR2 groups in the following metrics:* (**F**) distance travelled (ChR2 vs. eYFP: $p = 0.005$), (**G**) locomotor bouts (ChR2 vs. eYFP: $p = 0.005$), (**H**) movement speed (ChR2 vs. eYFP: $p < 0.001$) and (**I**) duration of locomotion in the open field (ChR2 vs. eYFP: $p < 0.001$). (**J**) The graph presents animal rotational bias using the turn angle sum. A significant increase in rotational bias was observed in 6-OHDA ChR2 mice during A13 region photoactivation (6-OHDA ChR2 vs. 6-OHDA eYFP: $p < 0.001$). (**K**) Diagram of the pole test. A mouse is placed facing upward on a vertical pole; "time to release" is defined as the interval from the experimenter removing their hand from the animal's tail to when the animal touches the ground. (**L, M**) Photoactivation of the A13 region decreased the time required to navigate to the base in 6-OHDA ChR2 mice compared to 6-OHDA eYFP mice ($p = 0.004$). A pre-op baseline was performed, followed by post-op testing three weeks later. On the experiment day, performance with no stimulation (Exp – NS) was compared to photoactivation (Exp – Stim). (**M**) 6-OHDA ChR2 mice showed a further reduction in time to reach the

base compared to 6-OHDA eYFP mice (6-OHDA ChR2 vs. 6-OHDA eYFP: $p < 0.001$). ***$p < 0.001$, **$p < 0.01$. Error bars indicate SEMs.

Next, we examined the reliability of photoactivation to initiate locomotion. The percentage of trials with at least one bout of locomotion was compared for the pre- and stim time points. 6-OHDA ChR2 animals showed a reliable pro-locomotion phenotype with A13 region photoactivation (Figure 3 -figure supplement 2A, $p = 0.042$). As was expected in the control 6-OHDA eYFP group, there was no effect of photoactivation on the probability of engaging in locomotion (Figure S3A, $p = 0.71$).

Movement speed contributes to total distance traveled and reflects the bradykinetic phenotype observed in 6-OHDA-lesioned mice (Magno et al., 2019; Sanders and Jaeger, 2016). The 6-OHDA and sham ChR2 groups displayed increases in average speed in comparison to the 6-OHDA and sham eYFP groups during photoactivation (Figure 3H, $p < 0.001$). There was no difference in the time to initiate locomotion between sham or 6-OHDA ChR2 groups (Figure 3 -figure supplement 2B, $p = 0.95$).

Photoactivation of the A13 region increases ipsilesional turning in the open field test

Unilateral 6-OHDA lesions drive asymmetric rotational bias (Boix et al., 2015; Li et al., 2022; Magno et al., 2019; Thiele et al., 2012). We investigated whether rotational bias persisted during photoactivation and observed that 6-OHDA ChR2 animals displayed increased ipsilesional rotation. Specifically, these animals showed a significant increase in turn angle sum (TAS), indicating enhanced rotational bias with photoactivation toward the lesioned side (Figure 3J, $p < 0.001$). As expected, 6-OHDA eYFP animals maintained a consistent rotational bias over time. To determine whether this effect was due to photoactivation alone or its interaction with the lesion, we also analyzed sham ChR2 animals. This group showed no significant change in TAS with photoactivation (Figure 3J, $p = 0.06$), suggesting that the effect is lesion-dependent. Next, we assessed whether the elevated TAS in 6-OHDA ChR2 animals occurred during locomotion. When TAS was calculated only during locomotor periods, the rotational bias was no longer observed. Instead, the increased rotational bias was evident between bouts of locomotor activity.

Skilled vertical locomotion is improved in the pole test with photoactivation of the A13 region.

The pole test is a well-established behavioral assay for 6-OHDA models (Figure 3K), requiring skilled locomotion for the animal to turn and descend a vertical pole (Matsuura et al., 1997; Ogawa et al., 1985). Improvements in function can be inferred if the time taken to complete the test decreases (Matsuura et al., 1997; Ogawa et al., 1985). 6-OHDA mice demonstrated significantly greater times navigating to the base than sham mice (Figure 3L, $p = 0.004$). Photoactivation of the A13 region led to shorter descent times to the base of the pole in 6-OHDA ChR2 mice compared to 6-OHDA eYFP mice (Figure 3L, $p = 0.004$, Movie S3). Neither of the eYFP groups showed any changes in the time to complete the pole test.

To isolate the effects of photoactivation on descent ability, we analyzed the time taken to descend after the turn, excluding delays from exploratory behavior at the top of the pole. While all groups showed reduced total pole test descent time with photoactivation, considering just the time to descend from turn alone, there was a larger improvement with A13 region photoactivation in the 6-OHDA ChR2 mice compared to 6-OHDA eYFP mice (Figure 3M, $p < 0.001$). These results indicate that photoactivation has the effect of reducing bradykinesia by improving the ability of mice to descend the pole during the pole test.

Dopaminergic Cells in the A13 region are preserved in the unilateral 6-OHDA mouse model

While photoactivation of the A13 region increased locomotor activity in both sham and 6-OHDA lesioned mice, we observed differences in speed and directional bias between the two groups. We hypothesized that these differences might be due to changes in the A13 region's connectome since previous research has shown that 6-OHDA lesions can lead to increases in firing frequency and metabolic activity in this brain region (Périer et al., 2000). To investigate this possibility, we used whole brain imaging approaches (Hansen et al., 2020; Zhan et al., 2021) to examine changes in the connectome following 6-OHDA lesions of the nigrostriatal pathway.

As expected (Iancu et al., 2005), our whole brain imaging results showed that TH^+ cells in SNc (Figure S4A-C) were more vulnerable to the 6-OHDA neurotoxin than those in the A13 (Figure 4B-F). Specifically, we found that 6-OHDA-treated mice showed a significantly greater percentage of TH^+ cell loss in SNc compared to the VTA and A13 (Figure 4G; VTA vs. SNc: $p < 0.01$; A13 vs. SNc: $p < 0.01$). In contrast, sham animals showed no change in TH^+ cell numbers across SNc, VTA and A13 (Figure S4G, $p > 0.05$). These findings are consistent with observations in the human brain, where the A13 region is preserved in the presence of extensive nigrostriatal degeneration (Matzuk and Saper, 1985). Our results confirm that the 6-OHDA mouse model effectively replicates this aspect of Parkinson's disease pathology.

Extensive Remodeling of the A13 Region Connectome Following Unilateral Nigrostriatal Degeneration

Although photoactivation of the A13 region was effective in restoring speed in 6-OHDA lesioned mice (Figure 3H), we observed an increase in circling behavior. This suggested that additional changes possibly reflecting alterations in the A13 connectome may be occurring. To investigate these potential changes without the potential confounds of an implanted optrode over the area, we conducted separate experiments to examine the changes in the input and output patterns of the A13 region in a small cohort of sham and 6-OHDA mice using whole-brain imaging approaches. We did this by co-injecting anterograde (AAV8-CamKII-mCherry) and retrograde AAV (AAVrg-CAG-GFP) tracers into the A13 nucleus (Paxinos and Franklin, 2008) (Figure 4). The injection core and spread were determined in the rostrocaudal direction from the injection site (Figure 4- figure supplement 1). The viral spread was centered around the mZI containing the A13, with minor spread to adjacent areas in some cases (Figure 4-figure supplement 1). To assess whether unilateral nigrostriatal degeneration led to changes in the organization of motor-related inputs and outputs from the A13, we first visualized interregional correlations of afferent and efferent proportions for each condition using correlation matrices (Figure 4A and B; 18 regions in a pairwise manner). The goal of this analysis was not to infer mechanistic pathways, but rather to provide a systems-level overview of how the global organization of A13 efferents and afferents is altered following 6-OHDA lesioning, highlighting how groups of regions co-vary in their input to or output from the A13 region. For example, a positive correlation between inputs from Region A and Region B to the A13 suggests that across animals, when input from Region A is relatively high, input from Region B tends to be high as well, indicating that connectivity from these regions to the A13 may be co-regulated or affected similarly by the lesion. Conversely, a shift from positive to negative correlation may signal a divergence in how regions contribute to the A13 connectome after nigrostriatal degeneration. Correlation matrices were organized using the hierarchical anatomical groups from the Allen Brain Atlas (Figure 5C-F). To control for experimental variations in the total labeling of neurons and fibers, we calculated the proportion of total inputs and outputs by dividing the afferent cell counts or efferent fiber areas in each brain region by the total number found in the brain. The data were then normalized to a $\log_{10}$

value to reduce variability and bring brain regions with high and low proportions of cells and fibers to a similar scale (Kimbrough et al., 2020). Comparing the afferent and efferent proportions pairwise between mice showed good consistency with an average correlation of 0.91 ± 0.02 (Spearman's correlation, Figure 6 - figure supplement 1).

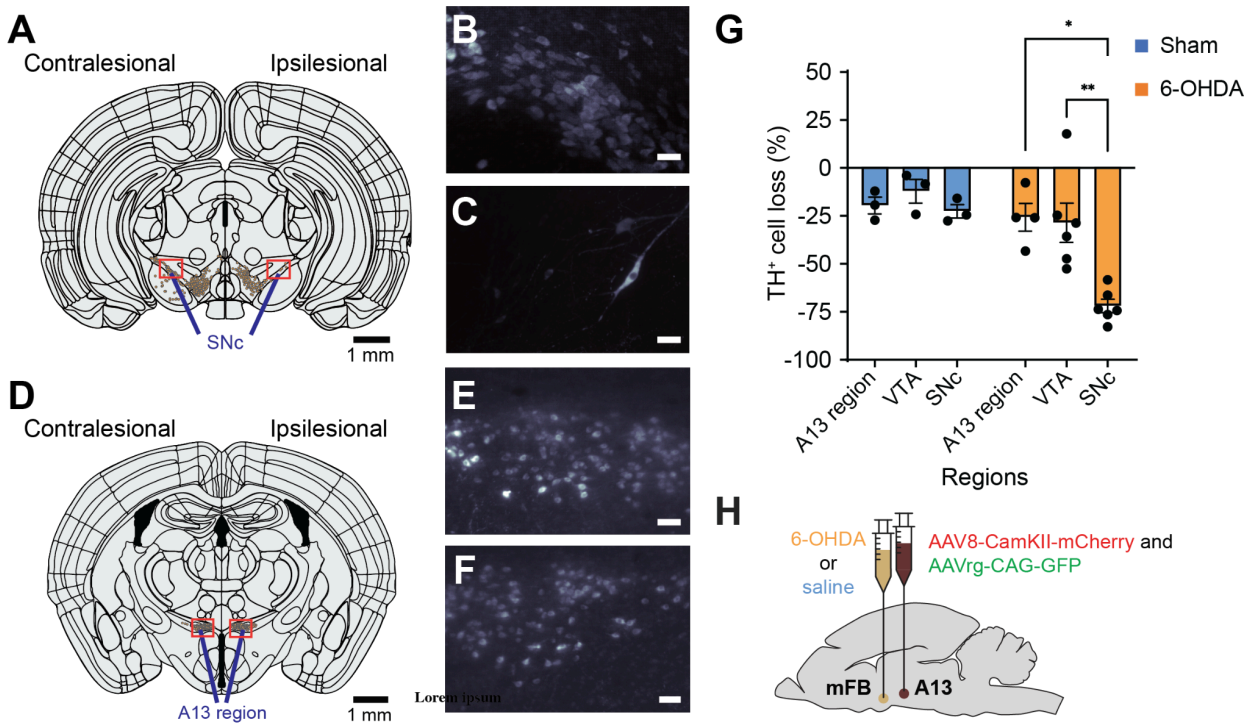

Figure 4. **Preservation of TH$^+$ A13 cells in Parkinsonian mouse models.** Representative slices of SNc (AP: -3.08 mm, **A**) and A13 region (AP: -1.355 mm, **D**) following registration with WholeBrain software. A There was a loss of TH$^+$ SNc cells following 6-OHDA injections at the MFB **(A)**. **(B, C)** Zoomed sections (90 µm thickness) of red boxes in panel A in left to right order. Meanwhile, TH$^+$ VTA cells were preserved bilaterally. Additionally, TH$^+$ A13 cells were present on the ipsilesional side to 6-OHDA injections **(D)**. **(E, F)** Zoomed sections (90 µm thickness) of red boxes in panel D in left to right order. When calculating the percentage of TH$^+$ cell loss normalized to the intact side, there was a significant interaction between the condition and brain region (repeated measures two-way ANOVA with *post hoc* Bonferroni pairwise, sham: n = 3, 6-OHDA: n = 6) **(G)** 6-OHDA-treated mice showed a significantly greater percentage of TH$^+$ cell loss in SNc compared to the VTA and A13 region (VTA vs. SNc: p = 0.005; A13 region vs. SNc: p = 0.03). In contrast, sham showed no significant difference in TH$^+$ cell loss across SNc, VTA and A13 regions ($p > 0.05$). *$p < 0.05$, and **$p < 0.01$. (**H**) Dual ipsilateral stereotaxic injection into the mFB and A13 region. Scale bars are 50 µm unless otherwise indicated.

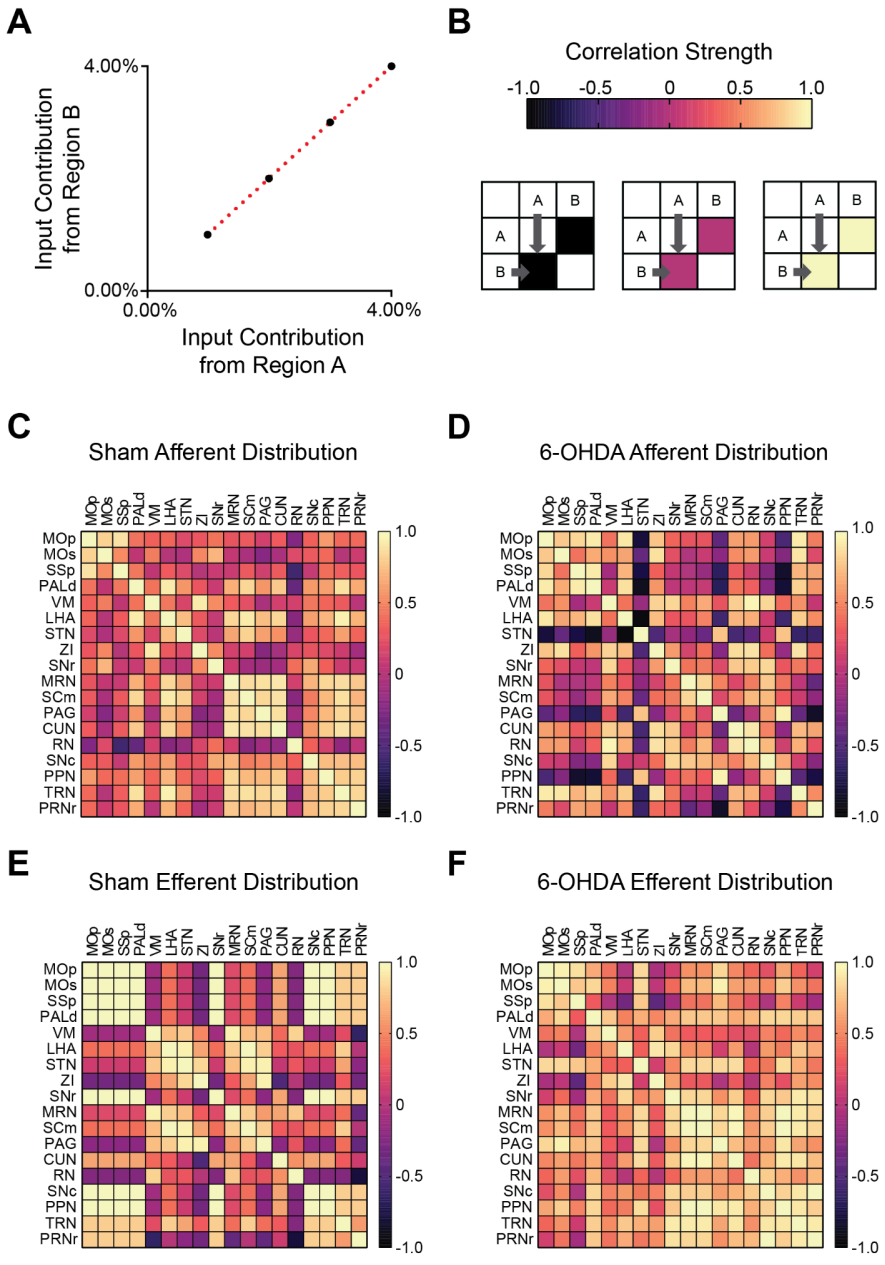

Figure 5. Nigrostriatal degeneration causes widespread changes in A13 region input and output connections. Correlation matrices were used to visualize the input and output patterns of the A13 region, focusing on motor-related pathways. **(A)** Brain regions with similar input patterns exhibit strong correlations. **(B)** Correlation strength is represented by cell color in the matrix: yellow indicates strong positive correlations, magenta denotes no correlation, and black indicates strong negative correlations. **(C, D)** Sham animals displayed stronger interregional correlations among inputs from motor-related regions across the neuraxis to the A13 region compared to 6-OHDA–lesioned mice. This suggests a broader distribution of inputs among motor-related cortical, subcortical, and brainstem regions in sham animals. **(D)** In 6-OHDA lesioned mice, inputs to the A13 region from the STN, PAG, and PPN became negatively correlated, unlike inputs from other motor-related regions. In contrast, inputs from motor-related pallidal and incertohypothalamic areas showed stronger positive correlations with cortical inputs, suggesting these regions may exert greater influence on A13 activity. **(E, F)** In contrast, output patterns from the A13 region showed stronger interregional correlations among cortical and brainstem motor-related regions in 6-OHDA–lesioned mice compared to sham animals. **(E)** In sham animals, A13 outputs to cortical regions were negatively correlated with outputs to thalamic, hypothalamic, and midbrain regions. This pattern was lost following nigrostriatal degeneration, suggesting a more distributed pattern of A13 outputs. MOp (primary motor cortex), MOs (secondary motor cortex), SSp (primary somatosensory area), PALd (pallidum, dorsal), VM (ventral medial thalamic nucleus), LHA (lateral hypothalamus), STN (subthalamic nucleus), ZI (zona incerta), SNr (substantia nigra pars reticulata), MRN (midbrain reticular nucleus), SCm (superior colliculus, motor), PAG (periaqueductal gray), CUN (cuneiform nucleus), RN (red nucleus), SNc (substantia nigra pars compacta), PPN (pedunculopontine nucleus), TRN (tegmental reticular nucleus), PRNr (pontine reticular nucleus).

We observed differences in afferent input patterns to the A13 region between sham and 6-OHDA groups. Correlation matrix analysis revealed that motor-related inputs to the A13 in sham animals exhibited stronger positive correlations across cortical, subcortical, and brainstem regions compared to 6-OHDA mice (Figure 5C). In 6-OHDA-lesioned mice, input distribution from dorsal pallidum, lateral hypothalamus, ZI, and tegmental reticular nucleus became positively correlated to somatomotor (MOp, MOs) and somatosensory (SSp) cortical areas (Figure 5D). Notably, these regions were anti-correlated with other motor-related inputs, indicating a reorganization of the afferent network. These data suggest a shift in the A13 inputs after 6-OHDA lesions, with a relative increase in cortical, pallidal, and hypothalamic influence compared to from other motor related brain regions.

In contrast, output patterns from the A13 region showed a higher overall correlation between brain regions in 6-OHDA-lesioned mice. In sham animals, A13 outputs to cortical regions were negatively correlated with outputs to thalamic, hypothalamic, and midbrain regions indicating a structured and selective projection pattern (Figure 5E). This specificity was lost (Figure 5F) in 6-OHDA mice, broader, less targeted distribution of A13 outputs following dopaminergic degeneration. These patterns offer new insight into the broader reorganization of the A13 connectome and may serve as systems-level signatures of altered anatomical organization, providing a foundation for future mechanistic investigations using circuit-specific tools. Future studies using cell type- and/or projection-specific functional manipulations will be essential to determine the causal roles of these reorganized circuits.

Differential remodeling of A13 region connectome ipsi- and contra-lesion following 6-OHDA-mediated nigrostriatal degeneration

We used whole-brain imaging to further investigate how the A13 connectome is affected by a unilateral 6-OHDA lesion. Our analysis revealed distinct patterns of remodelling on the lesioned (ipsilesional) and intact (contralesional) sides of the brain (Figure 6B, C, E, F). On the ipsilesional side, we observed a decrease in A13 afferent density in 6-OHDA mice compared to sham animals from several key regions (Figure 6A), including the primary motor cortex (MOp), primary somatosensory area (SSp), and secondary motor cortex (MOs). This reduced input from MOp, which is known for its role in initiating movement, could contribute to the initial bradykinesia observed in 6-OHDA mice. In contrast, ipsilesional compensatory increases in A13 afferents were observed, for example, from the lateral hypothalamic area (LHA), Substantia Nigra pars reticulata (SNr), Superior colliculus (SCm), and PAG. Examples are shown in Figure 6- figure supplement 1.

Interestingly, the contralesional side showed a more conservative pattern of afferent remodeling, with a modest decrease in A13 afferent density in primary motor cortex (MOp) and primary somatosensory cortex (SSp) of 6-OHDA mice, with a slight increase in the secondary motor cortex (MOs). For hypothalamic and midbrain structures only LHA and PAG showed evidence for an increase. Several regions, including the hypothalamus, midbrain, and pons showed bilateral upregulation of A13 afferents suggesting a more global compensatory response to the unilateral lesion.

Ipsilesional A13 efferents were decreased in 6-OHDA mice (Figure 6C) mainly in the somatosensory cortex (SSp; Figure 6A, Figure 6- figure supplement 2), with some modest increases in midbrain structures, whereas, contralesional efferent projection patterns showed increases in efferent density 6-OHDA mice compared to sham in cortical structures (MOp, MOs, SSp). This increase in efferent

projections to the contralesional motor cortices could explain the increased ipsilesional turning bias we observed during A13 photoactivation in the 6-OHDA group (Figure 3J). This was accompanied by modest decreases in efferent density in 6-OHDA contralesional midbrain structures compared to sham. Examples are shown in Figure 6- figure supplement 2.

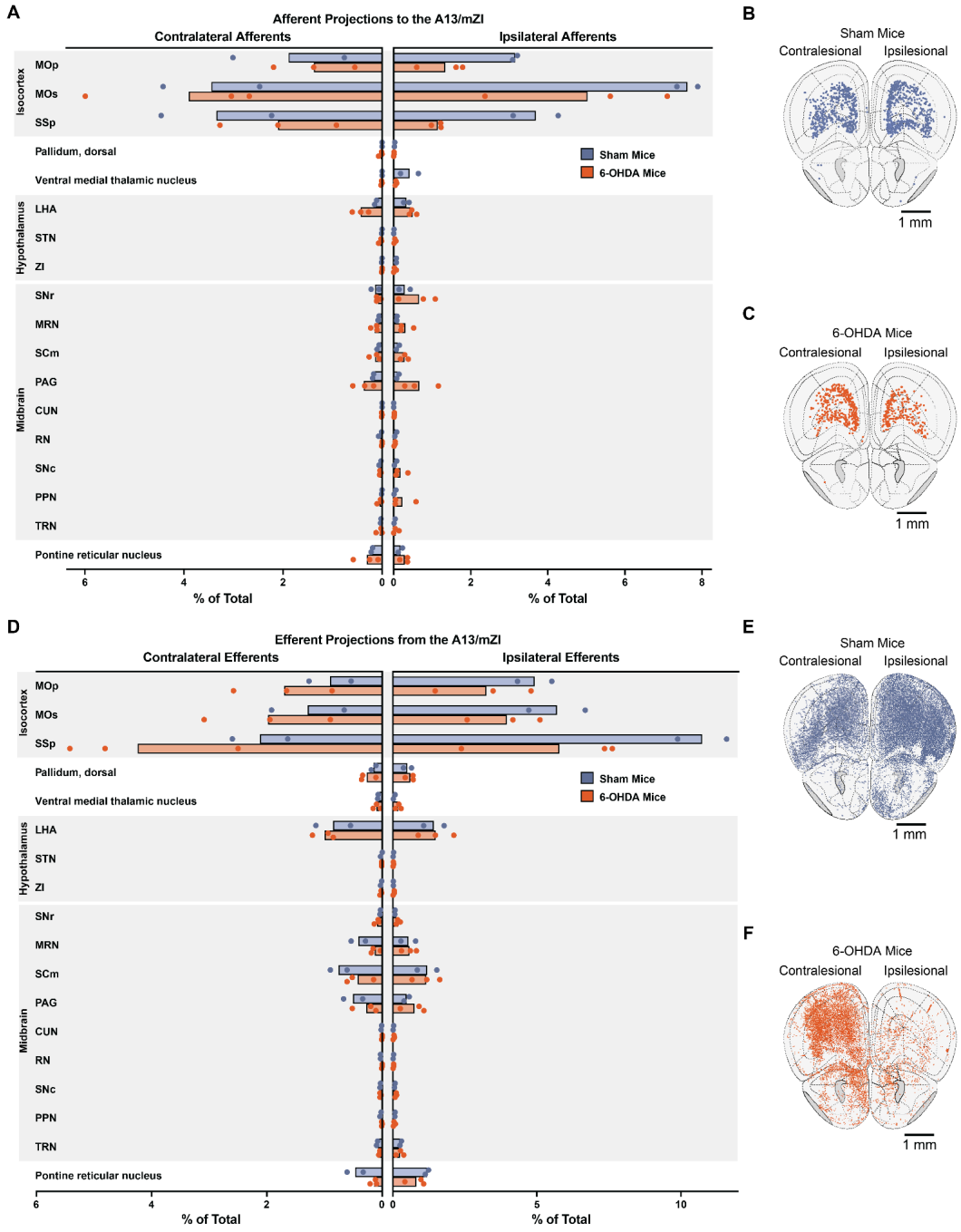

Figure 6. Unilateral nigrostriatal degeneration causes distinct changes in A13 connectivity.
(A) Relative changes in A13 afferent (input) connections in 6-OHDA-lesioned mice compared to sham controls. **(B, C)** Brain regions showing A13 input connections in sham **(B)** and 6-OHDA–lesioned **(C)** mice. **(D)** Relative changes in A13 efferent (output) connections in 6-OHDA-lesioned mice compared to sham controls. **(E, F)** Brain

regions showing A13 output connections in sham **(E)** and 6-OHDA–lesioned **(F)** mice. 6-OHDA: $n = 3$; sham: $n = 2$. Brain region abbreviations follow the Allen Brain Atlas: MOp (primary motor cortex), MOs (secondary motor cortex), SSp (primary somatosensory area), LHA (lateral hypothalamus), STN (subthalamic nucleus), ZI (zona incerta), SNr (substantia nigra pars reticulata), MRN (midbrain reticular nucleus), SCm (superior colliculus, motor), PAG (periaqueductal gray), CUN (cuneiform nucleus), RN (red nucleus), SNc (substantia nigra pars compacta), PPN (pedunculopontine nucleus), TRN (tegmental reticular nucleus).

DISCUSSION

This study aimed to determine whether activation of the A13 region could influence locomotor function, particularly in a PD model. Our results show that photoactivation of the A13 region enhances locomotion in both lesioned and sham mice, increasing distance traveled, locomotion time, and speed. Particularly in 6-OHDA mice, it rescued the number of locomotor bouts and significantly improved bradykinesia. Additionally, we observed remodeling of the A13 connectivity post-nigrostriatal lesions. These findings highlight the A13 region as a key area involved in locomotor control and suggest a potential therapeutic target for PD-related motor deficits.

The role of the A13 region in locomotion in sham mice

This study provides direct evidence that photoactivation of the A13 region can drive locomotion, suggesting that the pro-locomotor functions of the zona incerta extend further rostrally in the mouse. It adds to our work in rats where DBS of the A13 region evoked robust locomotor behavior (Bisht et al., 2025). Previous research has shown that photoactivation of caudal zona incerta (cZI) neurons increases animal movement speed in prey capture (Zhao et al., 2019) and active avoidance (Hormigo et al., 2020). Interestingly, early research on the cat suggested a role for the zona incerta in locomotion, particularly in the region adjacent to the subthalamic nucleus, but the effectiveness of rostral zona incerta regions containing the A13 was not reported (Grossman, 1958). Recent work shows that the A13 is involved in forelimb grasping (Garau et al., 2023), suggesting other motor control functions, while a positive valence associated with motivated food seeking behavior has also been reported (Ye et al., 2023). Previous work targeting the mZI region, including somatostatin (SOM^+), calretinin (CR^+), and $vGlut2^+$ neurons, did not change locomotor distance travelled in the OFT (Li et al., 2021). However, multiple populations being photostimulated or targeting more medial populations in the ZI may contribute to the differences. Our findings align with mini-endoscope recordings from $CaMKII\alpha^+$ rostral ZI cells, which overlap the A13 showing subpopulations whose activity correlates with either movement speed or anxiety-related locations (Li et al., 2021). Other work has found that photoactivation of GABAergic mZI pathways which project to the cuneiform promote exploratory activity by inhibiting cuneiform vGlut2 neurons (Sharma et al., 2024). There was a clear difference between the prolocomotor patterns observed after general mZI activation in this study and those resulting from the activation of mZI GABA populations. The activity patterns with CamII kinase promotor transfection of the region produced a marked effect on locomotor speed, accompanied by thigmotactic behaviors not observed when mZI GABAergic populations are activated. The pro-locomotor effects observed from the mZI region, both in this study and others, differ from those seen when lateral GABAergic ZI populations (dorsal and ventral ZI) are stimulated. Microinjection of $GABA_A$ receptor agonists into the ZI significantly reduces locomotor distance and velocity and may induce cataplexy. (Chen et al., 2023; Wardas et al., 1988). Alternatively, while suppressing GABAergic ZI activity with $GABA_A$ receptor antagonists can increase locomotion (Périer et al., 2002), chemogenetic or optogenetic inhibition in healthy naive mice can induce

bradykinesia and akinesia (Chen et al., 2023). These contrasting outcomes likely stem from the differing projection patterns of GABAergic populations.

The increased locomotor speed and improved descent times on the pole test, resulting from A13 region photoactivation, highlight its role in movement control. Given that A13 stimulation did not alter coordination during the task, it suggests a complex behavioral role consistent with its upstream location from the brainstem and its extensive afferent and efferent projections. Notably, A13 photoactivation also increased animal speed, duration, and distance traveled. Collectively, these findings represent a rescue of function in the 6-OHDA model. Interestingly, both 6-OHDA and sham mice exhibited a latency of 10 to 15 seconds on average following photoactivation before locomotion was initiated. Such delays are typical when stimulating sites upstream of the cuneiform, such as the dlPAG, which shows delays of several seconds (Tsang et al., 2021).

Photoactivation of the A13 reduces bradykinesia and akinesia in mouse PD models

While much work has targeted basal ganglia structures to address PD symptoms (DeLong and Wichmann, 2015), our research demonstrates that photoactivation of the A13 region can alleviate both bradykinesia and akinesia in 6-OHDA mice. Our work shows that A13 projections are affected at cortical and striatal levels following 6-OHDA, consistent with our observed changes in locomotor function. Over 28 days, there was a remarkable change in the afferent and efferent A13 connectome, despite the preservation of TH^+ ZI cells. This is consistent with previous reports of widespread connectivity of the ZI (Mitrofanis, 2005). The preservation of A13 is expected since A13 lacks DAT expression (Bolton et al., 2015; Negishi et al., 2020; Sharma et al., 2018) and is spared from DAT-mediated toxicity of 6-OHDA (Dauer and Przedborski, 2003; Konnova et al., 2018; Simola et al., 2007). While A13 cells were spared following nigrostriatal degeneration, our work demonstrates its connectome was rewired. The ipsilateral afferent projections were markedly downregulated, while contralesional projecting afferents showed upregulation. In contrast, efferent projections showed less downregulation in the cortical subplate regions and bilateral upregulation of thalamic and hypothalamic efferents. Similar timeframes for anatomical and functional plasticity affecting neurons and astrocytes following an SNc or mFB 6-OHDA have been previously reported (Bosson et al., 2015; Perović et al., 2005; Requejo et al., 2020). Human PD brains that show degeneration of the SNc have a preserved A13 region, suggesting that our model, from this perspective, is externally valid (Matzuk and Saper, 1985).

Combined with photoactivation of the A13 region, we provide evidence for plasticity following damage to SNc. A previous brain-wide quantification of TH levels in the MPTP mouse model identified additional complexity in regulating central TH expression compared to conventional histological studies (Roostalu et al., 2019). These authors reported decreased SNc TH^+ cell numbers without a significant change in TH^+ intensity in SNc and increased TH^+ intensity in limbic regions such as the amygdala and hypothalamus (Roostalu et al., 2019). Still, there was a downstream shift in the distribution pattern of A13 efferents following nigrostriatal degeneration with a reduction in outputs to cortical and striatal subregions. This suggests A13 efferents are more distributed across the neuraxis than in sham mice. One hypothesis arising from our work is that the preserved A13 efferents could provide compensatory innervation with collateralization mediated contralesionally and, in some subregions, ipsilesionally to increase the availability of extracellular dopamine.

Several A13 efferent targets could be responsible for rotational asymmetry. In a unilateral 6-OHDA model, ipsiversive circling behaviour is indicative of intact striatal function on the contralesional side (Carey, 1991; Schwarting et al., 1991; Ungerstedt, 1971; Zetterström et al., 1986). Instead, the predictive value of a treatment is determined by contraversive circling mediated by increased dopamine receptor sensitivity on the ipsilesional striatal terminals (Costall et al., 1976; Lane et al., 2006). Our findings show that A13 stimulation enhances ipsiversive circling and may represent a gain of function on the intact side, but this may be simply due to 6-OHDA mice having reduced locomotion overall. Given the preservation of A13 cells in PD, bilateral stimulation of A13 could potentially reduce motor asymmetry and alleviate bradykinesia and akinesia.

With the induction of a 6-OHDA lesion, there is a change in the A13 connectome, characterized by a reduction in bidirectional connectivity with ipsilesional cortical regions. In rodent models, the motor cortices, including the M1 and M2 regions, can shape rotational asymmetry (Gradinaru et al., 2009; Magno et al., 2019; Sanders and Jaeger, 2016; Valverde et al., 2020). Activation of M1 glutamatergic neurons increases the rotational bias (Valverde et al., 2020), while M2 neuronal stimulation promotes contraversive rotations (Magno et al., 2019). Our data suggest that A13 photoactivation may have resulted in the inhibition of glutamatergic neurons in the contralesional M1. An alternative possibility is the activation of the contralesional M2 glutamatergic neurons, which would be expected to induce increased ipsilesional rotations (Magno et al., 2019). The ZI could generate rotational bias by A13 modulation of cZI glutamatergic neurons via incerto-incertal fibers (Ossowska, 2020; Power and Mitrofanis, 1999), which promotes asymmetries by activating the SNr (Li et al., 2022). The incerto-incertal interconnectivity has not been well studied, but the ZI has a large degree of interconnectivity (Sharma et al., 2018; Tsang et al., 2021) along all axes and between hemispheres (Power and Mitrofanis, 1999). However, this may only contribute minimally given that unilateral photoactivation of the A13 cells in sham mice failed to produce ipsiversive turning behavior while unilateral photoactivation of cZI glutamatergic neurons in sham animals was sufficient in generating ipsiversive turning behavior (Li et al., 2022). Another possibility involves the A13 region projections to the MLR. With the unknown downstream effects of A13 photoactivation, there may be modulation of the PPN neurons responsible for this turning behavior (Masini and Kiehn, 2022). The thigmotactic behaviors suggest some effects may be mediated through dlPAG and CUN (Tsang et al., 2021), and recent work suggests the CUN as a possible therapeutic target (Fougère et al., 2021; Noga and Whelan, 2022). Since PD is a heterogeneous disease, our data provide another therapeutic target providing context-dependent relief from symptoms. This is important since PD severity, symptoms, and progression are patient-specific.

Towards a preclinical model

To facilitate future translational work applying DBS to this region, we targeted the A13 region using AAV8-CamKII-mCherry viruses. The CaMKIIα promoter virus is beneficial because it is biased towards excitatory cells (Haery et al., 2019), narrowing the diversity of the transfected A13 region and when combined with traditional therapies, such as L-DOPA, it could be a translatable strategy (Watakabe et al., 2015; Watanabe et al., 2020). Optogenetic strategies have been used to activate retinal cells in humans, partially restoring visual function and providing optimism that AAV-based viral strategies can be adapted in other human brain regions (Sahel et al., 2021). A more likely possibility for stimulation of deep nuclei is that DREADD technology could be adapted, which would not require any implants, however, this remains speculative. Our recent work demonstrates that the A13 is a target for DBS, where stimulation in

rats, as predicted, produced robust increases in locomotor activity (Bisht et al., 2025) . Gait dysfunction in PD is particularly difficult to treat, and indeed when DBS of subthalamic nucleus is deployed, a mixture of unilateral and bilateral approaches have been used (Lizarraga et al., 2016), along with stimulation of multiple targets (Stefani et al., 2007). This represents the heterogeneity of PD and underlines the need for considering multiple targets. DBS does not always have the same outcomes as optogenetic stimulation (Neumann et al., 2023), and our DBS shows a blend of anxiolytic and pro-locomotory effects, as predicted by this work and our work activating GABAergic mZI populations (Bisht et al., 2025; Sharma et al., 2024). Future work may want to consider a multipronged strategy to hone burst stimulation parameters with identification of cell populations to deploy DBS in a more targeted manner (Spix et al., 2021).

Limitations

Currently, few PD animal models are available that adequately model the progression and the extent of SNc cellular degeneration while meeting the face validity of motor deficits (Dauer and Przedborski, 2003; Konnova et al., 2018). While the 6-OHDA models fail to capture the age-dependent chronic degeneration observed in PD, they lead to robust motor deficits with acute degeneration and allow for compensatory changes in connectivity to be examined. Moreover, the 6-OHDA lesions resemble the unilateral onset (Hughes et al., 1992) and persistent asymmetry (Lee et al., 1995) of motor dysfunction in PD. Another option could be the MPTP mouse model, which offers the ease of systemic administration and translational value to primate models; however, the motor deficits are variable and lack the asymmetry observed in human patients (Hughes et al., 1992; Jagmag et al., 2015; Lee et al., 1995; Meredith and Rademacher, 2011). Despite these limitations, the neurotoxin-based mouse models, such as MPTP and 6-OHDA, offer greater SNc cell loss than genetic-based models; in the case of the 6-OHDA model, it captures many aspects of motor dysfunctions in PD (Dauer and Przedborski, 2003; Jagmag et al., 2015; Konnova et al., 2018; Simola et al., 2007). As in human PD, we found no significant change in A13 TH^+ cell counts (Matzuk and Saper, 1985). Another limitation is that since A13 neurons remained intact following a lesion, it is possible that changes in the connectome reflected secondary effects from other regions impacted by the 6-OHDA lesion. However, the fact that there was a significant change in the connectome post-6-OHDA injection and striatonigral degeneration is in and of itself important to document. Finally, it is important to note that our whole-brain anatomical data offer a correlative framework for understanding the neural circuits involved in A13-mediated locomotor control and its modulation in the 6-OHDA model. However, these data do not establish direct causal relationships. Future studies employing techniques such as targeted pathway manipulations (e.g., optogenetics, chemogenetics) or lesioning will be essential to definitively prove the functional necessity of specific connections in mediating the observed behavioral effects. A primary limitation of our whole-brain connectomic screen is the small sample size. This restricts the statistical power of our comparisons, and the imaging should be viewed as a preliminary, exploratory screen that provides valuable initial insights into the potential reorganization of the A13 connectome in the 6-OHDA model. Future studies with larger cohorts will be essential to confirm these findings. That said, the global approach allows us to identify widespread changes in connectivity that might be overlooked by more targeted analyses, offering insights into the complex neural adaptations that occur following nigrostriatal degeneration.

Conclusions

Our research underscores the role of the A13 region beyond the classic nigrostriatal axis in Parkinson's disease, driving locomotor activity and mitigating bradykinetic and akinetic deficits linked to impaired DAergic transmission. This observation indicates a rescue of locomotion loss in 6-OHDA-lesioned mice, as well as bradykinesia. Additionally, it produced possible gain-of-function effects, such as circling behavior, which may be attributed to plasticity changes induced by the 6-OHDA lesions. Widespread remodelling of the A13 region connectome is critical to our understanding of the effects of dopamine loss in PD models. In summary, our findings support an exciting role for the A13 region in locomotion with demonstrated benefits in a mouse PD model and contribute to our understanding of heterogeneity in PD.

MATERIALS AND METHODS

Key Resources Table				
Reagent type (species) or resource	**Designation**	**Source or reference**	**Identifiers**	**Additional information**
strain, strain background (*C57Bl/6 mice*)	**C57**	**Charles River**	**C57BL/6NCrl**	
antibody	**anti-cFos (Rabbit polyclonal)**	**Synaptic Systems**	**Cat# 226 003, RRID:AB_2231974**	**IF(1:1000), A13 region**
antibody	**anti-GFP (Chicken polyclonal)**	**Aves Lab**	**Cat# GFP-1010, RRID:AB_2307313**	**IF(1:1000), whole brain; IF(1:5000), A13 region**
antibody	**anti-mCherry (Rat monoclonal)**	**Invitrogen, Thermo Fisher Scientific**	**Cat# M11217; RRID:AB_2536611**	**IF(1:500), whole brain**
antibody	**anti-Tyrosine Hydroxylase (Rabbit polyclonal)**	**Abcam**	**Cat# AB-112, RRID:AB_2307313**	**IF(1:500), whole brain; IF(1:1000), SNc region**

antibody	anti-Tyrosine Hydroxylase (Sheep polyclonal)	Millipore Sigma	Cat# AB1542; RRID: AB_90755	IF(1:500), A13 region
antibody	Alexa Fluor® 488 Donkey Anti-Chicken	JacksonImmuno	703-545- 155	IF(1:200), whole brain; IF(1:1000) A13 region
antibody	Alexa Fluor® 594 Donkey Anti-Rabbit	Invitrogen, Thermo Fisher Scientific	A-21207	IF(1:500), A13 region
antibody	Alexa Fluor® 647 Donkey Anti-Rabbit	Invitrogen, Thermo Fisher Scientific	A-31573	IF(1:1000), SNc region
antibody	Alexa Fluor® 647 Donkey Anti-Sheep	Invitrogen, Thermo Fisher Scientific	A-21448	IF(1:1000), A13 region
antibody	Alexa Fluor® 790 Donkey Anti-Rabbit	Invitrogen, Thermo Fisher Scientific	A-11374	IF(1:200), whole brain
antibody	Cy™3 AffiniPure Donkey Anti-Rat	JacksonImmuno	712-165- 153	IF(1:200), whole brain
recombinant DNA reagent	AAV8-CamKII-mCherry	Neurophotonics	Cat# KD8-aav1	Lot #820, titre 2×10^{13} GC/ml
recombinant DNA reagent	AAVrg-CAG-GFP	Addgene	Cat# 37825	Lot #V9234, titre ≥ 7×10^{12} vg/mL

recombinant DNA reagent	AAVDJ-CaMKIIα-hChR2(H134R)- eYFP	UNC Stanford Viral Vector Core	Cat# AAV36	Lots #3081 and #6878, titres 1.9×10^{13} and 1.7×10^{13} GC/mL
recombinant DNA reagent	AAVDJ-CaMKIIα-eYFP	UNC Stanford Viral Vector Core	Cat# AAV08	Lots #2958 and #5510, titres 7.64×10^{13} and 2.88×10^{13} GC/mL
chemical compound, drug	Desipramine hydrochloride	Sigma Aldrich	D3900	2.5 mg/mL
chemical compound, drug	Pargyline hydrochloride	Sigma Aldrich	P8013	0.5 mg/mL
chemical compound, drug	6-OHDA	Tocris	2547/50	15.0 mg/mL
software, algorithm	Adobe Illustrator	Adobe	RRID:SCR_010279	
software, algorithm	ImageJ	ImageJ	RRID:SCR_003070	
software, algorithm	WholeBrain	WholeBrain	RRID:SCR_015245	
software, algorithm	Prism	GraphPad	RRID:SCR_002798	
software, algorithm	SPSS	SPSS	RRID:SCR_002865	

other	DAPI stain	Invitrogen, Thermo Fisher Scientific	D1306	IF(1:1000), A13/SNc regions
other	TO-PRO™-3 Iodide (642/661) stain	Invitrogen, Thermo Fisher Scientific	T3605	IF(1:5000), whole brain

Animals

All care and experimental procedures were approved by the University of Calgary Health Sciences Animal Care Committee (Protocol #AC19-0035). C57BL/6 male mice 49 - 56 days old (weight: M = 31.7 g, SEM = 2.0 g) were group-housed (< five per cage) on a 12-h light/dark cycle (07:00 lights on - 19:00 lights off) with *ad libitum* access to food and water, as well as cat's milk (Whiskas, Mars Canada Inc., Bolton, ON, Canada). Mice were randomly assigned to the groups described.

Surgical Procedures

We established a well-validated unilateral 6-OHDA mediated Parkinsonian mouse model (Thiele et al., 2012) (Figure 1). 30 minutes before stereotaxic microinjections, mice were intraperitoneally injected with desipramine hydrochloride (2.5 mg/ml, Sigma-Aldrich) and pargyline hydrochloride (0.5 mg/ml, Sigma-Aldrich) at 10 ml/kg (0.9% sterile saline, pH 7.4) to enhance selectivity and efficacy of 6-OHDA induced lesions (Thiele et al., 2012). All surgical procedures were performed using aseptic techniques, and mice were anesthetized using isoflurane (1 - 2%) delivered by 0.4 L/min of medical-grade oxygen (Vitalair 1072, 100% oxygen).

Mice were stabilized on a stereotaxic apparatus. Small craniotomies were made above the medial forebrain bundle (mFB) and the A13 nucleus within one randomly assigned hemisphere. Stereotaxic microinjections were performed using a glass capillary (Drummond Scientific, PA, USA; Puller Narishige, diameter 15 – 20 mm) and a Nanoject II apparatus (Drummond Scientific, PA, USA). 240 nL of 6-OHDA (3.6 µg, 15.0 mg/mL; Tocris, USA) was microinjected into the MFB (AP -1.2 mm from bregma; ML ±1.1 mm; DV -5.0 mm from the dura). Sham mice received a vehicle solution (240 nL of 0.2% ascorbic acid in 0.9% saline; Tocris, USA).

Whole Brain Experiments

For tracing purposes, a 50:50 mix of AAV8-CamKII-mCherry (Neurophotonics, Laval University, Quebec City, Canada, Lot #820, titre 2×10^{13} GC/ml) and AAVrg-CAG-GFP (Addgene, Watertown, MA, Catalogue #37825, Lot #V9234, titre $\geq 7\times10^{12}$ vg/mL) was injected ipsilateral to 6-OHDA injections at the A13 nucleus in all mice (AP -1.22 mm from bregma; ML ±0.4 mm; DV -4.5 mm from the dura, the total volume of 110 nL at a rate of 23 nL/s). Post-surgery care was the same for both sham and 6-OHDA injected mice. The animals were sacrificed 29 days after surgery.

Photoactivation Experiments

36.8 nL of AAVDJ-CaMKIIα-hChR2(H134R)-eYFP (UNC Stanford Viral Gene Core; Stanford, CA, US, Catalogue #AAV36; Lots #3081 and #6878, titres 1.9×10^{13} and 1.7×10^{13} GC/mL, respectively) or eYFP

control virus (AAVDJ-CaMKIIα-eYFP; Lots #2958 and #5510, titres 7.64×10^{13} and 2.88×10^{13} GC/mL, respectively) were injected into the A13 (AP: -1.22 mm; ML -0.5 mm from the Bregma; DV -4.5 mm from the dura). A mono-fiber cannula (Doric Lenses, Quebec, Canada, Catalogue #B280-2401-5, MFC_200/230-0.48_5mm_MF2.5_FLT) was implanted slowly 300 µm above the viral injection site. Metabond® Quick Adhesive Cement System (C&B, Parkell, Brentwood, NY, US) and Dentsply Repair Material (Dentsply International Inc., York, PA, USA) were used to fix the optical fiber in place. Animals recovered from the viral surgery for 19 days before follow-up behavioral testing. Figure 1 shows a timeline of behavioral tests.

ChR2 photoactivation

Photoactivation was achieved using a 473 nm laser and driver (LRS-0473-GFM-00100-05, Laserglow Technologies, North York, ON, Canada). The laser was triggered by TTL pulses from an A.M.P.I. Master-8 stimulator (Jerusalem, Israel) or an Open Ephys PulsePal (Sanworks, Rochester, NY, US) set to 20 Hz, 10-ms pulse width and 5 mW power. All fiber optic implants were tested for laser power before implantation (Thorlabs, Saint-Laurent, QC, Canada; optical power sensor (S130C) and meter (PM100D)). The Stanford Optogenetics irradiance calculator was used to estimate the laser power for stimulation ("Stanford Optogenetics Resource Center," n.d.). A 1×2 fiber-optic rotary joint (Doric Lenses, Quebec, Canada; FRJ_1x2i_FC-2FC_0.22) was used. The animals' behaviors were recorded with an overhead camera (SuperCircuits, Austin, TX, US; FRJ_1x2i_FC-2FC_0.22; 720 x 480 resolution; 30 fps). The video was processed online (Cleversys, Reston, VA; TopScan V3.0) with a TTL signal output from a National Instruments 24-line digital I/O box (NI, Austin, TX, US; USB-6501) to the Master-8 stimulator.

Behavioral Testing

Open Field Test

Each mouse was placed in a square arena measuring 70 (W) x 70 (L) x 50 (H) cm with opaque walls and recorded for 30 minutes using a vertically mounted video camera (Model PC165DNR, Supercircuits, Austin, TX, USA; 30 fps). 19 days following surgery, mice were habituated to the open field test (OFT) arena with a patch cable attached for three days in 30 minute sessions to bring animals to a common baseline of activity. On experimental days, after animals were placed in the OFT, a one-minute-on-three-minutes-off paradigm was repeated five times following an initial ten minutes baseline activity. Locomotion was registered when mice traveled a minimum distance of 10 cm at 6 cm/s for 20 frames over a 30-frame segment. When the mouse velocity dropped below 6 cm/s for 20 frames, locomotion was recorded as ending. Bouts of locomotion relate to the number of episodes where the animal met these criteria. Velocity data were obtained from the frame-by-frame results and further processed in a custom Python script to detect instantaneous speeds greater than 2 cm/s (Masini and Kiehn, 2022). All animals that had validated targeting of the A13 region were included in the OFT data presented in the results section, except for one sham ChR2 animal, which showed grooming rather than the typical locomotor phenotypes.

Pole Test

Mice were placed on a vertical wooden pole (50 cm tall and 1 cm diameter) facing upwards and then allowed to descend the pole into their home cage (Glajch et al., 2012). Animals were trained for three days and tested 2-5 days pre-surgery. Animals were acclimatized 21-22 days post-surgery under two conditions: without a patch cable and with the patch cable attached without photoactivation. On days

24-27, experimental trials were recorded with photoactivation. Video data were recorded for a minimum of three trials (Canon, Brampton, ON, Canada; Vixia HF R52; 1920 x 1080 resolution; 60 fps). A blinded scorer recorded the times for the following events: the hand release of the animal's tail, the animal fully turning to descend the pole, and the animal reaching the base of the apparatus. Additionally, partial falls, where the animal slipped down the pole but did not reach the base, and full falls, where the animal fell to the base, were recorded separately. All validated animals were included in the quantified data, including the sham ChR2 animal that began grooming in the OFT upon photoactivation. This animal displayed proficiency in performing the pole test during photoactivation. It started grooming upon completion of the task when photoactivation was on. One sham ChR2 animal was photostimulated at 1 mW since it would jump off the apparatus at higher stimulation intensities.

Immunohistochemistry

A13 and SNc region

Post hoc analysis of the tissue was performed to confirm the 6-OHDA lesion and validate the targeting of the A13 region. Following behavioral testing, animals underwent a photoactivation protocol to activate neurons below the fiber optic tip (Koblinger et al., 2018). Animals were placed in an OFT for ten minutes before receiving three minutes of photoactivation. Ten minutes later, the animals were returned to their home cage. 90 minutes post photoactivation, animals were deeply anesthetized with isoflurane and then transcardially perfused with room temperature PBS followed by cold 4% paraformaldehyde (PFA) (Sigma-Aldrich, Catalogue #441244-1KG). The animals were decapitated, and the whole heads were incubated overnight in 4% PFA at 4°C before the fiber optic was removed and the brain removed from the skull. The brain tissue was post-fixed for another 6 - 12 hours in 4% PFA at 4°C then transferred to 30% sucrose solution for 48 - 72 hours. The tissue was embedded in VWR® Clear Frozen Section Compound (VWR International LLC, Radnor, PA, US) and sectioned coronally at 40 or 50 µm using a Leica cryostat set to -21°C (CM 1850 UV, Concord, ON, Canada). Sections from the A13 region (-0.2 to -2.0 mm past bregma) and the SNc (-2.2 to -4.0 mm past bregma) were collected and stored in PBS containing 0.02% (w/v) sodium azide (EM Science, Catalogue #SX0299-1, Cherry Hill, NJ, US) (Paxinos and Franklin, 2008).

Immunohistochemistry staining was done on free-floating sections. The A13 sections were labelled for c-Fos, TH, and GFP (to enhance eYFP viral signal), and received a DAPI stain to identify nuclei. The SNc sections were stained with TH and DAPI. Sections were washed in PBS (3 x 10 mins) then incubated in a blocking solution comprised of PBS containing 0.5% Triton X-100 (Sigma-Aldrich, Catalogue #X100-500ML, St. Louis, MO, US) and 5% donkey serum (EMD Millipore, Catalogue #S30-100ML, Billerica, MA, USA) for 1 hour. This was followed by overnight (for SNc sections) or 24-hour (for A13 sections) incubation in a 5% donkey serum PBS primary solution at room temperature. On day 2, the tissue was washed in PBS (3 x 10 mins) before being incubated in a PBS secondary solution containing 5% donkey serum for 2 hours (for SNc tissue) or 4 hours (for A13 tissue). The secondary was washed with a PBS solution containing 1:1000 DAPI for 10 mins, followed by a final set of PBS washes (3 x 10 mins). Tissue was mounted on Superfrost® micro slides (VWR, slides, Radnor, PA, US) with mounting media (Vectashield®, Vector Laboratories Inc., Burlingame, CA, US), covered with #1 coverslips (VWR, Radnor, PA, US) then sealed.

Whole Brain

Mice were deeply anesthetized with isoflurane and transcardially perfused with PBS, followed by 4% PFA. To prepare for whole brain imaging, brains were first extracted and postfixed overnight in 4% PFA at 4°C. The next day, a modified iDISCO method (Renier et al., 2014) was used to clear the samples and perform quadruple immunohistochemistry in whole brains. The modifications include prolonged incubation and the addition of SDS for optimal labelling. Antibodies used are listed in the Key Resources Table and the protocol is provided in Whole Brain Clearing Protocol

.

Whole Brain Clearing Protocol

Day #	Instructions
1	Washed 2 x 30 minutes in PBS on a shaker at room temperature.
2	Dehydrated tissue in methanol/H_2O series of 20%, 40%, 60%, 80%, 100%, 100% (1 hour each at room temperature) then left overnight in a 66% dichloromethane/33% methanol solution.
3	Washed twice in 100% methanol at room temperature and then chilled the samples at 4°C. Bleached the samples in chilled fresh 5% H_2O_2 in methanol (1 volume 30% H_2O_2 to 5 volumes methanol), overnight at 4°C.
4	Rehydrated in methanol/water series of 80%, 60%, 40%, 20%, PBS (1 hour each at room temperature). Washed twice in PTx.2 (0.2% Triton™ X-100 in PBS). Incubated the samples in Permeabilization Solution at 37°C for 2 days.
6	Washed 3 x 1-2 hours in 0.5mM SDS/PBS at 37°C then incubated for 3 days.
9	Incubated with the primary antibody in 0.5mM SDS/PBS at 37°C for 3 days.
12	Refreshed with the primary antibody in PTx.2 at 37°C then incubated for 4 days.
17	Washed 5 x 2 hours in PTwH (0.2% Tween® 20 and 10 mg/mL Heparin stock solution in PBS) and incubated at 37°C overnight.
18	Incubated with secondary antibody in PTwH/3% Donkey Serum at 37°C for 3 days.
21	Refreshed with secondary antibody in PTwH/3% Donkey Serum at 37°C for 4 days.
25	Washed 5 x 2 hours in PTwH then incubated at 37°C overnight.

26 Dehydrated in methanol/water series of 20%, 40%, 60%, 80%, 100% (1 hour each at room temperature). Refreshed the samples with 100 % methanol and left overnight at room temperature.

27 Incubated in 66% DCM/33% methanol for 3 hours on a shaker at room temperature. Then incubated in 100% DCM (Sigma 270997-12X100ML) for 2 x 15 minutes (with shaking) to wash away methanol. Incubated samples with ethyl cinnamate for 3 hours at room temperature with shaking. Refreshed ethyl cinnamate then left at room temperature for imaging.

Image Acquisition and Analysis

Photoactivation Experiments

All tissue was initially scanned with an Olympus VS120-L100 Virtual Slide Microscope (UPlanSApo, 10x and 20x, NA = 0.4 and 0.75). Standard excitation and emission filter cube sets were used (DAPI, FITC, TRITC, Cy5), and images were acquired using an Orca Flash 4.0 sCMOS monochrome camera (Hamamatsu, Bridgewater Township, NJ, US). For c-Fos immunofluorescence, A13 sections of the tissue were imaged with a Leica SP8 FALCON (FAst Lifetime CONtrast) scanning confocal microscope equipped with a tunable laser and using a 63x objective (HC PlanApo, NA = 1.40).

SNc images were imported into Adobe Illustrator, where the SNc (Fougère et al., 2021), including the pars lateralis (SNl), was delineated using the TH immunostaining together with the medial lemniscus and cerebral peduncle as landmarks (bregma -3.09 and -3.68 mm) (Iancu et al., 2005; Paxinos and Franklin, 2008; Stott and Barker, 2014). Cell counts were obtained using a semi-automated approach using an Ilastik (v1.4.0b15) (Berg et al., 2019) trained model followed by corrections by a blinded counter (Fougère et al., 2021; Iancu et al., 2005). Targeting was confirmed on the 10x overview scans of the A13 region tissue by the presence of eYFP localized in the mZI around the A13 TH^+ nucleus, the fiber optic tip being visible near the mZI and A13 nucleus, and the presence of c-Fos positive cells in $ChR2^+$ tissue. C-Fos expression colocalization within the A13 region was performed using confocal images. The mZI & A13 region was identified with the 3rd ventricle and TH expression as markers (Paxinos and Franklin, 2008).

Whole Brain Experiments

Cleared whole brain samples were imaged using a light-sheet microscope (LaVision Biotech UltraMicroscope, LaVision, Bielefeld, Germany) with an Olympus MVPLAPO 2x objective with 4x optical zoom (NA = 0.475) and a 5.7 mm dipping cap that is adjusted for the high refractive index of 1.56. The brain samples were imaged in an ethyl cinnamate medium to match the refractive indices and illuminated by three sheets of light bilaterally. Each light sheet was 5 µm thick, and the width was set at 30% to ensure sufficient illumination at the centroid of the sample. Laser power intensities and chromatic aberration corrections used for each laser were as follows: 10 % power for 488 nm laser, 5% power for 561 nm laser with 780 nm correction, 40 % power for 640 nm laser with 960 nm correction, and 100 % power for 785 nm laser with 1,620 nm correction. Each sample was imaged coronally in 8 by 6 squares with 20% overlap (10,202 µm by 5,492 µm in total) and a z-step size of 15 µm (xyz resolution = 0.813 µm x 0.813 µm x 15 µm). While an excellent choice for our work, confocal microscopy offers better

resolution at the expense of time. To gain a better resolution using a light-sheet microscope in select regions (eg. SNc and A13 cells), we increased the optical zoom to 6.3x.

A13 Connectome Analysis

Images were processed using ImageJ software (Schneider et al., 2012). Raw images were stitched, and a z-encoded maximum intensity projection across a 90 µm thick optical section was obtained across each brain. 90 µm sections were chosen because the 2008 Allen reference atlas images are spaced out at around 100 µm. Brains with insufficient quality in labeling were excluded from analysis (n = 1 of three sham and n = 3 of six 6-OHDA mice). Instructions for identifying YFP^+ or TH^+ cells to annotate were provided to the manual counters. YFP^+ and TH^+ cells were manually counted using the Cell Counter Plug-In (ImageJ). $mCherry^+$ fibers were segmented semi-automatically using Ilastik software (Berg et al., 2019) and quantified using particle analysis in ImageJ. Images and segmentations were imported into WholeBrain software to be registered with the 2008 Allen reference atlas (Fürth et al., 2018). The TO-PRO™-3 and TH channels were used as reference channels to register each section to a corresponding atlas image. ImageJ quantifications of cell and fiber segmentations were exported in XML formats and registered using WholeBrain software. To minimize the influence of experimental variation on the total labeling of neurons and fibers, the afferent cell counts or efferent fiber areas in each brain region were column divided by the total number found in a brain to obtain the proportion of total inputs and outputs. Connectome analyses were performed using custom R scripts. For interregional correlation analyses, the data were normalized to a $\log_{10}$ value to reduce variability and bring brain regions with high and low proportions of cells and fibers to a similar scale. The consistency of afferent and efferent proportions between mice was compared in a pairwise manner using Spearman's correlation (Figure S6).

Quantification of 6-OHDA mediated TH^+ cell loss.

The percentage of TH^+ cell loss was quantified to confirm 6-OHDA mediated SNc lesions. TH^+ cells within ZI, VTA and SNc areas from 90 µm thick optical brain slice images (AP: -0.655 to -3.88 mm from bregma) were manually counted by two blinded counters (n = 3 sham and n = 6 6-OHDA mice; ZI region in 2 of 6 6-OHDA mice were excluded due to presence of abnormal scarring/healing at the injection site of viruses). Subsequently, WholeBrain software (Fürth et al., 2018) was used to register and tabulate TH^+ cells in the contralesional and ipsilesional brain regions of interest. Counts obtained from the two counters were averaged per region. The percentage of TH^+ cell loss was calculated by dividing the difference in counts between contralesional and ipsilesional sides by the contralesional side count and multiplying by 100 %.

Statistical analyses

All data were tested for normality using a Shapiro-Wilk test to determine the most appropriate statistical tests. The percent ipsilesional TH^+ neuron loss within the SNc as defined above using a Pearson correlation (Fougère et al., 2021) was used to ascertain the effect of the 6-OHDA lesion on behavior. A Wilcoxon rank-sum test was performed for comparisons within subjects at two timepoints where normality failed, and the central limit theorem could not be applied. The two groups were compared using an unpaired t-test with Welch's correction. A mixed model ANOVA (MM ANOVA) was used to compare the effects of group type, injection type and time. Additionally, Mauchly's test of sphericity was performed to account for differences in variability within the repeated measures design. A Greenhouse Geisser correction was applied to all ANOVAs where Mauchly's test was significant for RM and MM

ANOVAs. The *post hoc* multiple comparisons were run when the respective ANOVAs reached significance using Dunnett's or Dunn's tests for repeated measures of parametric and non-parametric tests, respectively. The pre-stimulation timepoints were used as the control time point to determine if stimulation altered behavior. A Bonferroni correction was added for *post hoc* comparisons following a MM ANOVA between groups at given time points to control for alpha value inflation. All correlations, t-tests, and ANOVAs were performed, and graphs were created using Prism version 9.3.1 (Graphpad) or SPSS (IBM, 28.0.1.0). Full statistical reporting is in Supplemental Statistics.xls.

Figures

Figures were constructed using Adobe Photoshop, Illustrator, and Biorender.

ACKNOWLEDGEMENTS

We would like to acknowledge support from Whelan and Kiss Labs and technical support from Hotchkiss Brain Institute Advanced Microscopy Platform Core Facility, Cumming School of Medicine Optogenetics Platform Core Facility and Drs. David Elliot, Jonathan Epp, Young Ou, and Lothar Resch. We acknowledge studentships from Parkinson Alberta (LHK), Parkinson Canada (LHK), Canadian Open Neuroscience Platform (AL), Cumming School of Medicine (AL, LHK), Faculty of Graduate Studies (AL, LHK), and the Faculty of Veterinary Medicine (CM, ST). This research was supported by grants to PJW provided by a Canadian Institutes of Health Research Project Grant (PJT-173511), Wings for Life, NSERC (RGPIN/04394-2019) as well as ZHTK from NSERC (RPGIN/04126-2017).

DATA AVAILABILITY

All datasets and code have been deposited at Open Science Framework (OSF).

REFERENCES

Berg S, Kutra D, Kroeger T, Straehle CN, Kausler BX, Haubold C, Schiegg M, Ales J, Beier T, Rudy M, Eren K, Cervantes JI, Xu B, Beuttenmueller F, Wolny A, Zhang C, Koethe U, Hamprecht FA, Kreshuk A. 2019. ilastik: interactive machine learning for (bio)image analysis. *Nat Methods* **16**:1226–1232.

Bisht A, Badenhorst C, Kiss Z, Murari K, Whelan P. 2025. Deep brain stimulation of A13 region evokes robust locomotory response in rats. *J Neurophysiol*. doi:10.1152/jn.00019.2025

Blomstedt P, Stenmark Persson R, Hariz G-M, Linder J, Fredricks A, Häggström B, Philipsson J, Forsgren L, Hariz M. 2018. Deep brain stimulation in the caudal zona incerta versus best medical treatment in patients with Parkinson's disease: a randomised blinded evaluation. *J Neurol Neurosurg Psychiatry* **89**:710–716.

Boix J, Padel T, Paul G. 2015. A partial lesion model of Parkinson's disease in mice--characterization of a 6-OHDA-induced medial forebrain bundle lesion. *Behav Brain Res* **284**:196–206.

Bolton AD, Murata Y, Kirchner R, Kim S-Y, Young A, Dang T, Yanagawa Y, Constantine-Paton M. 2015. A Diencephalic Dopamine Source Provides Input to the Superior Colliculus, where D1 and D2 Receptors Segregate to Distinct Functional Zones. *Cell Rep* **13**:1003–1015.

Bosson A, Boisseau S, Buisson A, Savasta M, Albrieux M. 2015. Disruption of dopaminergic transmission remodels tripartite synapse morphology and astrocytic calcium activity within substantia nigra pars reticulata. *Glia* **63**:673–683.

Braak H, Del Tredici K, Rüb U, de Vos RAI, Jansen Steur ENH, Braak E. 2003. Staging of brain pathology related to sporadic Parkinson's disease. *Neurobiol Aging* **24**:197–211.

Caire F, Ranoux D, Guehl D, Burbaud P, Cuny E. 2013. A systematic review of studies on anatomical position of electrode contacts used for chronic subthalamic stimulation in Parkinson's disease. *Acta Neurochir* **155**:1647–54; discussion 1654.

Carey RJ. 1991. Chronic L-dopa treatment in the unilateral 6-OHDA rat: evidence for behavioral sensitization and biochemical tolerance. *Brain Res* **568**:205–214.

Cenci MA, Björklund A. 2020. Animal models for preclinical Parkinson's research: An update and critical appraisal. *Prog Brain Res* **252**:27–59.

Chen F, Qian J, Cao Z, Li A, Cui J, Shi L, Xie J. 2023. Chemogenetic and optogenetic stimulation of zona incerta GABAergic neurons ameliorates motor impairment in Parkinson's disease. *iScience* **26**. doi:10.1016/j.isci.2023.107149

Choi EA, McNally GP. 2017. Paraventricular Thalamus Balances Danger and Reward. *J Neurosci* **37**:3018–3029.

Chometton S, Charrière K, Bayer L, Houdayer C, Franchi G, Poncet F, Fellmann D, Risold PY. 2017. The rostromedial zona incerta is involved in attentional processes while adjacent LHA responds to arousal: c-Fos and anatomical evidence. *Brain Struct Funct* **222**:2507–2525.

Costall B, Naylor RJ, Pycock C. 1976. Non-specific supersensitivity of striatal dopamine receptors after 6-hydroxydopamine lesion of the nigrostriatal pathway. *Eur J Pharmacol* **35**:276–283.

Dauer W, Przedborski S. 2003. Parkinson's disease: mechanisms and models. *Neuron* **39**:889–909.

DeLong MR, Wichmann T. 2015. Basal Ganglia Circuits as Targets for Neuromodulation in Parkinson Disease. *JAMA Neurol* **72**:1354–1360.

Eaton MJ, Wagner CK, Moore KE, Lookingland KJ. 1994. Neurochemical identification of A13 dopaminergic neuronal projections from the medial zona incerta to the horizontal limb of the diagonal band of Broca and the central nucleus of the amygdala. *Brain Res* **659**:201–207.

Ferraye MU, Debû B, Fraix V, Goetz L, Ardouin C, Yelnik J, Henry-Lagrange C, Seigneuret E, Piallat B, Krack P, Le Bas J-F, Benabid A-L, Chabardès S, Pollak P. 2010. Effects of pedunculopontine nucleus area stimulation on gait disorders in Parkinson's disease. *Brain* **133**:205–214.

Fougère M, van der Zouwen CI, Boutin J, Neszvecsko K, Sarret P, Ryczko D. 2021. Optogenetic stimulation of glutamatergic neurons in the cuneiform nucleus controls locomotion in a mouse model of Parkinson's disease. *Proc Natl Acad Sci U S A* **118**. doi:10.1073/pnas.2110934118

Fürth D, Vaissière T, Tzortzi O, Xuan Y, Märtin A, Lazaridis I, Spigolon G, Fisone G, Tomer R, Deisseroth K, Carlén M, Miller CA, Rumbaugh G, Meletis K. 2018. An interactive framework for whole-brain maps at cellular resolution. *Nat Neurosci* **21**:139–149.

Garau C, Hayes J, Chiacchierini G, McCutcheon JE, Apergis-Schoute J. 2023. Involvement of A13 dopaminergic neurons in prehensile movements but not reward in the rat. *Curr Biol*. doi:10.1016/j.cub.2023.09.044

Glajch KE, Fleming SM, Surmeier DJ, Osten P. 2012. Sensorimotor assessment of the unilateral 6-hydroxydopamine mouse model of Parkinson's disease. *Behav Brain Res* **230**:309–316.

Glickstein M, Stein J. 1991. Paradoxical movement in Parkinson's disease. *Trends Neurosci* **14**:480–482.

Goldowitz D. 2010. Allen Reference Atlas. A Digital Color Brain Atlas of the C57BL/6J Male Mouse - by H. W. Dong. *Genes, Brain and Behavior*. doi:10.1111/j.1601-183x.2009.00552.x

Gradinaru V, Mogri M, Thompson KR, Henderson JM, Deisseroth K. 2009. Optical deconstruction of parkinsonian neural circuitry. *Science* **324**:354–359.

Grossman RG. 1958. Effects of stimulation of non-specific thalamic system on locomotor movements in cat. *J Neurophysiol* **21**:85–93.

Gut NK, Winn P. 2015. Deep Brain Stimulation of Different Pedunculopontine Targets in a Novel Rodent Model of Parkinsonism. *Journal of Neuroscience*. doi:10.1523/jneurosci.3646-14.2015

Haery L, Deverman BE, Matho KS, Cetin A, Woodard K, Cepko C, Guerin KI, Rego MA, Ersing I, Bachle SM, Kamens J, Fan M. 2019. Adeno-Associated Virus Technologies and Methods for Targeted Neuronal Manipulation. *Front Neuroanat* **13**:93.

Hamani C, Moro E, Lozano AM. 2011. The pedunculopontine nucleus as a target for deep brain stimulation. *J Neural Transm* **118**:1461–1468.

Hansen HH, Roostalu U, Hecksher-Sørensen J. 2020. Whole-brain three-dimensional imaging for quantification of drug targets and treatment effects in mouse models of neurodegenerative diseases. *Neural Regeneration Res* **15**:2255–2257.

Hoffman BJ, Palkovits M, Paiak K, Hamson SR, Mezey É. 1997. Regulation of Dopamine Transporter mRNA Levels in the Central Nervous System In: Goldstein DS, Eisenhofer G, McCarty R, editors. Advances in Pharmacology. Academic Press. pp. 202–206.

Hormigo S, Zhou J, Castro-Alamancos MA. 2020. Zona Incerta GABAergic Output Controls a Signaled Locomotor Action in the Midbrain Tegmentum. *eNeuro* **7**. doi:10.1523/ENEURO.0390-19.2020

Hughes AJ, Ben-Shlomo Y, Daniel SE, Lees AJ. 1992. What features improve the accuracy of clinical diagnosis in Parkinson's disease: a clinicopathologic study. *Neurology* **42**:1142–1146.

Iancu R, Mohapel P, Brundin P, Paul G. 2005. Behavioral characterization of a unilateral 6-OHDA-lesion model of Parkinson's disease in mice. *Behav Brain Res* **162**:1–10.

Jagmag SA, Tripathi N, Shukla SD, Maiti S, Khurana S. 2015. Evaluation of Models of Parkinson's Disease. *Front Neurosci* **9**:503.

Ji Y-W, Zhang X, Fan J-P, Gu W-X, Shen Z-L, Wu H-C, Cui G, Zhou C, Xiao C. 2023. Differential remodeling of subthalamic projections to basal ganglia output nuclei and locomotor deficits in 6-OHDA-induced hemiparkinsonian mice. *Cell Rep* **42**:112178.

Kimbrough A, Lurie DJ, Collazo A, Kreifeldt M, Sidhu H, Macedo GC, D'Esposito M, Contet C, George O. 2020. Brain-wide functional architecture remodeling by alcohol dependence and abstinence. *Proc Natl Acad Sci U S A* **117**:2149–2159.

Kim LH, Chomiak T, Tran MA, Tam S, McPherson C, Eaton SEA, Ou Y, Kiss ZHT, Whelan PJ. 2021. Global remodelling of afferent and efferent projections of the A13 region following unilateral nigrostriatal degeneration using 6-hydroxydopamineNeuroscience Meeting Planner. Presented at the Society for Neuroscience. Society for Neuroscience.

Kim LH, Sharma S, Sharples SA, Mayr KA, Kwok CHT, Whelan PJ. 2017. Integration of Descending Command Systems for the Generation of Context-Specific Locomotor Behaviors. *Front Neurosci* **11**:581.

Kish SJ, Tong J, Hornykiewicz O, Rajput A, Chang L-J, Guttman M, Furukawa Y. 2008. Preferential loss of serotonin markers in caudate versus putamen in Parkinson's disease. *Brain* **131**:120–131.

Koblinger K, Jean-Xavier C, Sharma S, Füzesi T, Young L, Eaton SEA, Kwok CHT, Bains JS, Whelan PJ. 2018. Optogenetic Activation of A11 Region Increases Motor Activity. *Front Neural Circuits* **12**:86.

Konnova EA, Translational Neurogenetics Unit, Wallenberg Neuroscience Center, Lund University, Lund, Sweden, Swanberg M, Translational Neurogenetics Unit, Wallenberg Neuroscience Center, Lund University, Lund, Sweden. 2018. Animal models of Parkinson's diseaseParkinson's Disease: Pathogenesis and Clinical Aspects. Codon Publications. pp. 83–106.

Lane EL, Cheetham SC, Jenner P. 2006. Does contraversive circling in the 6-OHDA-lesioned rat indicate an ability to induce motor complications as well as therapeutic effects in Parkinson's disease? *Exp Neurol* **197**:284–290.

Lee CS, Schulzer M, Mak E, Hammerstad JP, Calne S, Calne DB. 1995. Patterns of asymmetry do not change over the course of idiopathic parkinsonism: implications for pathogenesis. *Neurology* **45**:435–439.

Li L-X, Li Y-L, Wu J-T, Song J-Z, Li X-M. 2022. Glutamatergic neurons in the caudal Zona incerta regulate parkinsonian motor symptoms in mice. *Neurosci Bull* **38**:1–15.

Lim S-Y, Fox SH, Lang AE. 2009. Overview of the extranigral aspects of Parkinson disease. *Arch Neurol* **66**:167–172.

Li S, Shi Y, Kirouac GJ. 2014. The hypothalamus and periaqueductal gray are the sources of dopamine fibers in the paraventricular nucleus of the thalamus in the rat **8**:136.

Lizarraga KJ, Jagid JR, Luca CC. 2016. Comparative effects of unilateral and bilateral subthalamic nucleus deep brain stimulation on gait kinematics in Parkinson's disease: a randomized, blinded study. *J Neurol* **263**:1652–1656.

Li Z, Rizzi G, Tan KR. 2021. Zona incerta subpopulations differentially encode and modulate anxiety. *Sci Adv* **7**:eabf6709.

Magno LAV, Tenza-Ferrer H, Collodetti M, Aguiar MFG, Rodrigues APC, da Silva RS, Silva J do P, Nicolau NF, Rosa DVF, Birbrair A, Miranda DM, Romano-Silva MA. 2019. Optogenetic Stimulation of the M2 Cortex Reverts Motor Dysfunction in a Mouse Model of Parkinson's Disease. *J Neurosci* **39**:3234–3248.

Masini D, Kiehn O. 2022. Targeted activation of midbrain neurons restores locomotor function in mouse models of parkinsonism. *Nat Commun* **13**:504.

Matsuura K, Kabuto H, Makino H, Ogawa N. 1997. Pole test is a useful method for evaluating the mouse movement disorder caused by striatal dopamine depletion. *J Neurosci Methods* **73**:45–48.

Matzuk MM, Saper CB. 1985. Preservation of hypothalamic dopaminergic neurons in Parkinson's disease. *Ann Neurol* **18**:552–555.

Meredith GE, Rademacher DJ. 2011. MPTP mouse models of Parkinson's disease: an update. *J Parkinsons Dis* **1**:19–33.

Messanvi F, Eggens-Meijer E, Roozendaal B, van der Want JJ. 2013. A discrete dopaminergic projection from the incertohypothalamic A13 cell group to the dorsolateral periaqueductal gray in rat. *Front Neuroanat* **7**:41.

Mitrofanis J. 2005. Some certainty for the "zone of uncertainty"? Exploring the function of the zona incerta. *Neuroscience* **130**:1–15.

Mitrofanis J, Mikuletic L. 1999. Organisation of the cortical projection to the zona incerta of the thalamus. *J Comp Neurol* **412**:173–185.

Mok D, Mogenson GJ. 1986. Contribution of zona incerta to osmotically induced drinking in rats. *Am J Physiol* **251**:R823–32.

Monosov IE, Ogasawara T, Haber SN, Heimel JA, Ahmadlou M. 2022. The zona incerta in control of novelty seeking and investigation across species. *Curr Opin Neurobiol* **77**:102650.

Moriya S, Yamashita A, Masukawa D, Setoyama H, Hwang Y, Yamanaka A, Kuwaki T. 2020. Involvement of A13 dopaminergic neurons located in the zona incerta in nociceptive processing: a fiber photometry study. *Mol Brain* **13**:60.

Moro E, Hamani C, Poon Y-Y, Al-Khairallah T, Dostrovsky JO, Hutchison WD, Lozano AM. 2010.

Unilateral pedunculopontine stimulation improves falls in Parkinson's disease. *Brain* **133**:215–224.
Negishi K, Payant MA, Schumacker KS, Wittmann G, Butler RM, Lechan RM, Steinbusch HWM, Khan AM, Chee MJ. 2020. Distributions of hypothalamic neuron populations coexpressing tyrosine hydroxylase and the vesicular GABA transporter in the mouse. *J Comp Neurol* **528**:1833–1855.
Neumann W-J, Steiner LA, Milosevic L. 2023. Neurophysiological mechanisms of deep brain stimulation across spatiotemporal resolutions. *Brain* **146**:4456–4468.
Noga BR, Whelan PJ. 2022. The Mesencephalic Locomotor Region: Beyond Locomotor Control. *Front Neural Circuits* **16**:884785.
Nonnekes J, Bereau M, Bloem BR. 2020. Freezing of Gait and Its Levodopa Paradox. *JAMA Neurol* **77**:287–288.
Nonnekes J, Snijders AH, Nutt JG, Deuschl G, Giladi N, Bloem BR. 2015. Freezing of gait: a practical approach to management. *Lancet Neurol* **14**:768–778.
Ogawa N, Hirose Y, Ohara S, Ono T, Watanabe Y. 1985. A simple quantitative bradykinesia test in MPTP-treated mice. *Res Commun Chem Pathol Pharmacol* **50**:435–441.
Ogundele OM, Lee CC, Francis J. 2017. Thalamic dopaminergic neurons projects to the paraventricular nucleus-rostral ventrolateral medulla/C1 neural circuit. *The Anatomical Record*. doi:10.1002/ar.23528
Okun MS, Foote KD. 2010. Parkinson's disease DBS: what, when, who and why? The time has come to tailor DBS targets. *Expert Rev Neurother* **10**:1847–1857.
Ossowska K. 2020. Zona incerta as a therapeutic target in Parkinson's disease. *J Neurol* **267**:591–606.
Paxinos G, Franklin KBJ. 2008. The mouse brain in stereotaxic coordinates, compact: The coronal plates and diagrams, 3rd ed. San Diego, CA: Academic Press.
Peoples C, Spana S, Ashkan K, Benabid A-L, Stone J, Baker GE, Mitrofanis J. 2012. Photobiomodulation enhances nigral dopaminergic cell survival in a chronic MPTP mouse model of Parkinson's disease. *Parkinsonism Relat Disord* **18**:469–476.
Perez-Lloret S, Barrantes FJ. 2016. Deficits in cholinergic neurotransmission and their clinical correlates in Parkinson's disease. *NPJ Parkinsons Dis* **2**:16001.
Périer C, Tremblay L, Féger J, Hirsch EC. 2002. Behavioral consequences of bicuculline injection in the subthalamic nucleus and the zona incerta in rat. *J Neurosci* **22**:8711–8719.
Périer C, Vila M, Féger J, Agid Y, Hirsch EC. 2000. Functional activity of zona incerta neurons is altered after nigrostriatal denervation in hemiparkinsonian rats. *Exp Neurol* **162**:215–224.
Perović M, Mladenović A, Rakić L, Ruzdijić S, Kanazir S. 2005. Increase of GAP-43 in the rat cerebellum following unilateral striatal 6-OHDA lesion. *Synapse* **56**:170–174.
Plaha P, Khan S, Gill SS. 2008. Bilateral stimulation of the caudal zona incerta nucleus for tremor control. *J Neurol Neurosurg Psychiatry* **79**:504–513.
Power BD, Mitrofanis J. 1999. Evidence for extensive inter-connections within the zona incerta in rats. *Neurosci Lett* **267**:9–12.
Renier N, Wu Z, Simon DJ, Yang J, Ariel P, Tessier-Lavigne M. 2014. iDISCO: a simple, rapid method to immunolabel large tissue samples for volume imaging. *Cell* **159**:896–910.
Requejo C, López-de-Ipiña K, Ruiz-Ortega JÁ, Fernández E, Calvo PM, Morera-Herreras T, Miguelez C, Cardona-Grifoll L, Cepeda H, Ugedo L, Lafuente JV. 2020. Changes in Day/Night Activity in the 6-OHDA-Induced Experimental Model of Parkinson's Disease: Exploring Prodromal Biomarkers. *Front Neurosci* **14**:590029.
Roostalu U, Salinas CBG, Thorbek DD, Skytte JL, Fabricius K, Barkholt P, John LM, Jurtz VI, Knudsen LB, Jelsing J, Vrang N, Hansen HH, Hecksher-Sørensen J. 2019. Quantitative whole-brain 3D imaging of tyrosine hydroxylase-labeled neuron architecture in the mouse MPTP model of Parkinson's disease. *Dis Model Mech* **12**. doi:10.1242/dmm.042200
Sahel J-A, Boulanger-Scemama E, Pagot C, Arleo A, Galluppi F, Martel JN, Delaux A, de Saint Aubert J-B, de Montleau C, Gutman E, Audo I, Duebel J, Picaud S, Dalkara D, Blouin L, Taiel M, Roska B. 2021. Partial recovery of visual function in a blind patient after optogenetic therapy. *Nat Med* **27**:1223–1229.

Sanders TH, Jaeger D. 2016. Optogenetic stimulation of cortico-subthalamic projections is sufficient to ameliorate bradykinesia in 6-ohda lesioned mice. *Neurobiol Dis* **95**:225–237.

Sanghera MK, Anselmo-Franci J, McCann SM. 1991. Effect of Medial Zona Incerta Lesions on the Ovulatory Surge of Gonadotrophins and Prolactin in the Rat. *Neuroendocrinology*. doi:10.1159/000125931

Sanghera MK, Grady S, Smith W, Woodward DJ, Porter JC. 1991. Incertohypothalamic A13 dopamine neurons: effect of gonadal steroids on tyrosine hydroxylase. *Neuroendocrinology* **53**:268–275.

Scatton B, Javoy-Agid F, Rouquier L, Dubois B, Agid Y. 1983. Reduction of cortical dopamine, noradrenaline, serotonin and their metabolites in Parkinson's disease. *Brain Res* **275**:321–328.

Schneider CA, Rasband WS, Eliceiri KW. 2012. NIH Image to ImageJ: 25 years of image analysis. *Nat Methods* **9**:671–675.

Schwarting RK, Bonatz AE, Carey RJ, Huston JP. 1991. Relationships between indices of behavioral asymmetries and neurochemical changes following mesencephalic 6-hydroxydopamine injections. *Brain Res* **554**:46–55.

Sharma S, Badenhorst CA, Ashby DM, Di Vito SA, Tran MA, Ghavasieh Z, Grewal GK, Belway CR, McGirr A, Whelan PJ. 2024. Inhibitory medial zona incerta pathway drives exploratory behavior by inhibiting glutamatergic cuneiform neurons. *Nat Commun* **15**:1160.

Sharma S, Kim LH, Mayr KA, Elliott DA, Whelan PJ. 2018. Parallel descending dopaminergic connectivity of A13 cells to the brainstem locomotor centers. *Sci Rep* **8**:7972.

Shaw VE, Spana S, Ashkan K, Benabid A-L, Stone J, Baker GE, Mitrofanis J. 2010. Neuroprotection of midbrain dopaminergic cells in MPTP-treated mice after near-infrared light treatment. *J Comp Neurol* **518**:25–40.

Simola N, Morelli M, Carta AR. 2007. The 6-hydroxydopamine model of Parkinson's disease. *Neurotox Res* **11**:151–167.

Sita LV, Elias CF, Bittencourt JC. 2007. Connectivity pattern suggests that incerto-hypothalamic area belongs to the medial hypothalamic system **148**:949–969.

Spix TA, Nanivadekar S, Toong N, Kaplow IM, Isett BR, Goksen Y, Pfenning AR, Gittis AH. 2021. Population-specific neuromodulation prolongs therapeutic benefits of deep brain stimulation. *Science* **374**:201–206.

Stanford Optogenetics Resource Center. n.d. https://web.stanford.edu/group/dlab/cgi-bin/graph/chart.php

Stefani A, Lozano AM, Peppe A, Stanzione P, Galati S, Tropepi D, Pierantozzi M, Brusa L, Scarnati E, Mazzone P. 2007. Bilateral deep brain stimulation of the pedunculopontine and subthalamic nuclei in severe Parkinson's disease. *Brain* **130**:1596–1607.

Stott SRW, Barker RA. 2014. Time course of dopamine neuron loss and glial response in the 6-OHDA striatal mouse model of Parkinson's disease. *Eur J Neurosci* **39**:1042–1056.

Thevathasan W, Debu B, Aziz T, Bloem BR, Blahak C, Butson C, Czernecki V, Foltynie T, Fraix V, Grabli D, Joint C, Lozano AM, Okun MS, Ostrem J, Pavese N, Schrader C, Tai C-H, Krauss JK, Moro E, Movement Disorders Society PPN DBS Working Groupin collaboration with the World Society for Stereotactic and Functional Neurosurgery. 2018. Pedunculopontine nucleus deep brain stimulation in Parkinson's disease: A clinical review. *Mov Disord* **33**:10–20.

Thiele SL, Warre R, Nash JE. 2012. Development of a unilaterally-lesioned 6-OHDA mouse model of Parkinson's disease. *J Vis Exp*. doi:10.3791/3234

Tsang E, Orlandini C, Sureka R, Crevenna AH, Perlas E, Prankerd I, Masferrer ME, Gross CT. 2021. Induction of flight via midbrain projections to the cuneiform nucleus. *bioRxiv*. doi:10.1101/2021.12.21.473683

Ungerstedt U. 1971. Striatal dopamine release after amphetamine or nerve degeneration revealed by rotational behaviour. *Acta Physiol Scand Suppl* **367**:49–68.

Valverde S, Vandecasteele M, Piette C, Derousseaux W, Gangarossa G, Aristieta Arbelaiz A, Touboul J, Degos B, Venance L. 2020. Deep brain stimulation-guided optogenetic rescue of parkinsonian symptoms. *Nat Commun* **11**:2388.

Venkataraman A, Hunter SC, Dhinojwala M, Ghebrezadik D, Guo J, Inoue K, Young LJ, Dias BG. 2021.

Incerto-thalamic modulation of fear via GABA and dopamine. *Neuropsychopharmacology* **46**:1658–1668.

Wang X, Chou X-L, Zhang LI, Tao HW. 2020. Zona Incerta: An Integrative Node for Global Behavioral Modulation. *Trends Neurosci* **43**:82–87.

Wardas J, Ossowska K, Wolfarth S. 1988. Evidence for the independent role of GABA synapses of the zona incerta-lateral hypothalamic region in haloperidol-induced catalepsy. *Brain Res* **462**:378–382.

Watakabe A, Ohtsuka M, Kinoshita M, Takaji M, Isa K, Mizukami H, Ozawa K, Isa T, Yamamori T. 2015. Comparative analyses of adeno-associated viral vector serotypes 1, 2, 5, 8 and 9 in marmoset, mouse and macaque cerebral cortex. *Neurosci Res* **93**:144–157.

Watanabe H, Sano H, Chiken S, Kobayashi K, Fukata Y, Fukata M, Mushiake H, Nambu A. 2020. Forelimb movements evoked by optogenetic stimulation of the macaque motor cortex. *Nat Commun* **11**:3253.

Yang Y, Jiang T, Jia X, Yuan J, Li X, Gong H. 2022. Whole-Brain Connectome of GABAergic Neurons in the Mouse Zona Incerta. *Neurosci Bull* **38**:1315–1329.

Ye Q, Nunez J, Zhang X. 2023. Zona incerta dopamine neurons encode motivational vigor in food seeking. *Sci Adv* **9**:eadi5326.

Zetterström T, Herrera-Marschitz M, Ungerstedt U. 1986. Simultaneous measurement of dopamine release and rotational behaviour in 6-hydroxydopamine denervated rats using intracerebral dialysis. *Brain Res* **376**:1–7.

Zhan Y, Wu H, Liu L, Lin J, Zhang S. 2021. Organic solvent-based tissue clearing techniques and their applications. *J Biophotonics* **14**:e202000413.

Zhao Z-D, Chen Z, Xiang X, Hu M, Xie H, Jia X, Cai F, Cui Y, Chen Z, Qian L, Liu J, Shang C, Yang Y, Ni X, Sun W, Hu J, Cao P, Li H, Shen WL. 2019. Zona incerta GABAergic neurons integrate prey-related sensory signals and induce an appetitive drive to promote hunting. *Nat Neurosci* **22**:921–932.

Zweig RM, Jankel WR, Hedreen JC, Mayeux R, Price DL. 1989. The pedunculopontine nucleus in Parkinson's disease. *Ann Neurol* **26**:41–46.

FIGURE SUPPLEMENTS

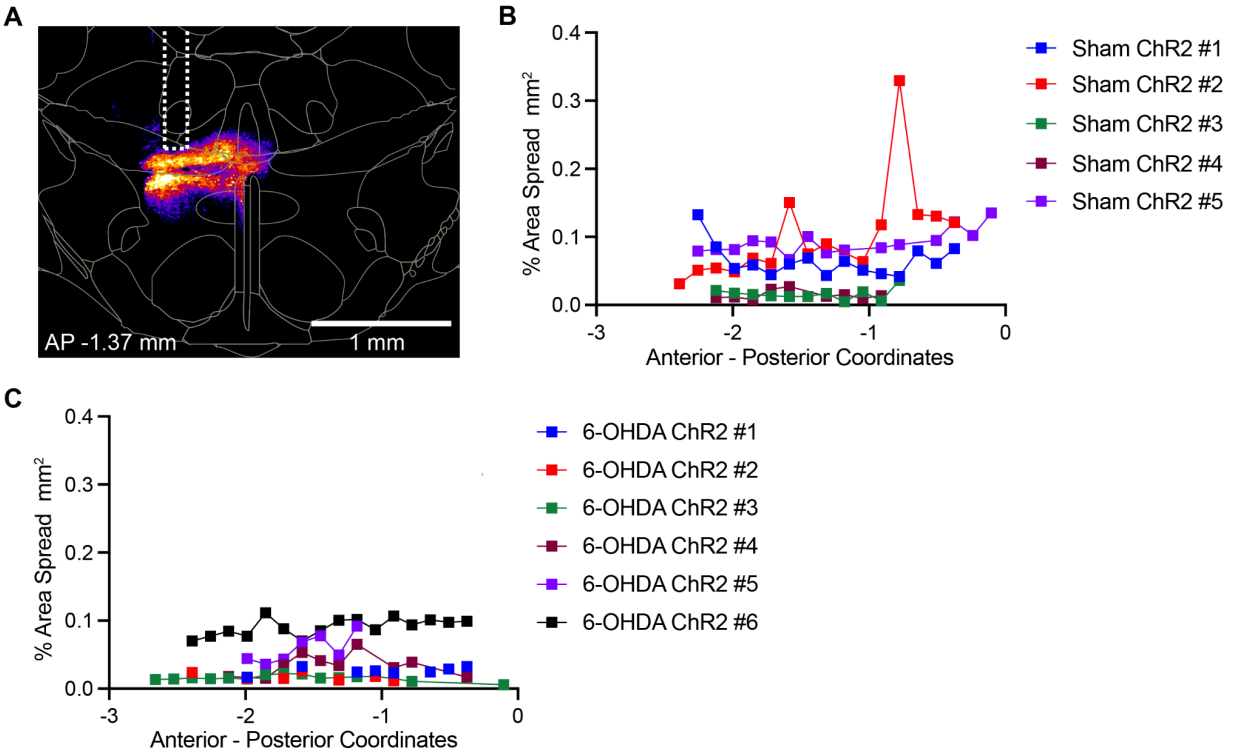

Figure 2 - figure supplement 1. Quantification of channelrhodopsin viral spread in the rostral-caudal direction from the injection site in 6-OHDA-treated and sham animals. A. A representative image of viral spread, including the optic fiber track, visualized using the "fire" lookup table in FIJI/ImageJ software. Targeting precision was confirmed by coronal overlays from the Mouse Allen Brain Atlas onto the A1xxxx3 region. **B, C.** Graphs illustrating the percentage of viral spread across anterior–posterior coordinates for ChR2-transfected Sham **(B)**, and 6-OHDA **(C)** mice, calculated as the ratio of viral expression area to total tissue section area. Data were obtained from brain sections of mice injected with AAVDJ-CaMKIIα-ChR2 into the A13 region, sectioned at 50 µm, and analyzed using the VS120 Virtual Slide Scanner. Quantification was performed by blinded analysts using FIJI/ImageJ with defined regions of interest (ROIs).

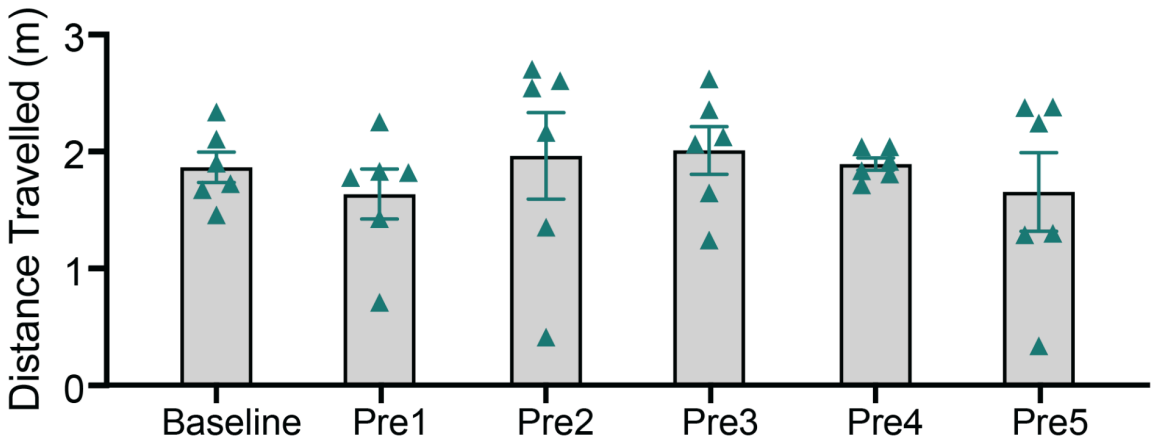

Figure 3 - figure supplement 1. Time course of open-field locomotion distance traveled over 30 minutes. Locomotion distance traveled for the six sham ChR2 animals at baseline and across five pre-stimulation timepoints was compared using a one-way repeated-measures ANOVA ($F_{5,25} = 0.49$, $p = 0.78$). Data are presented as mean ± SEM.

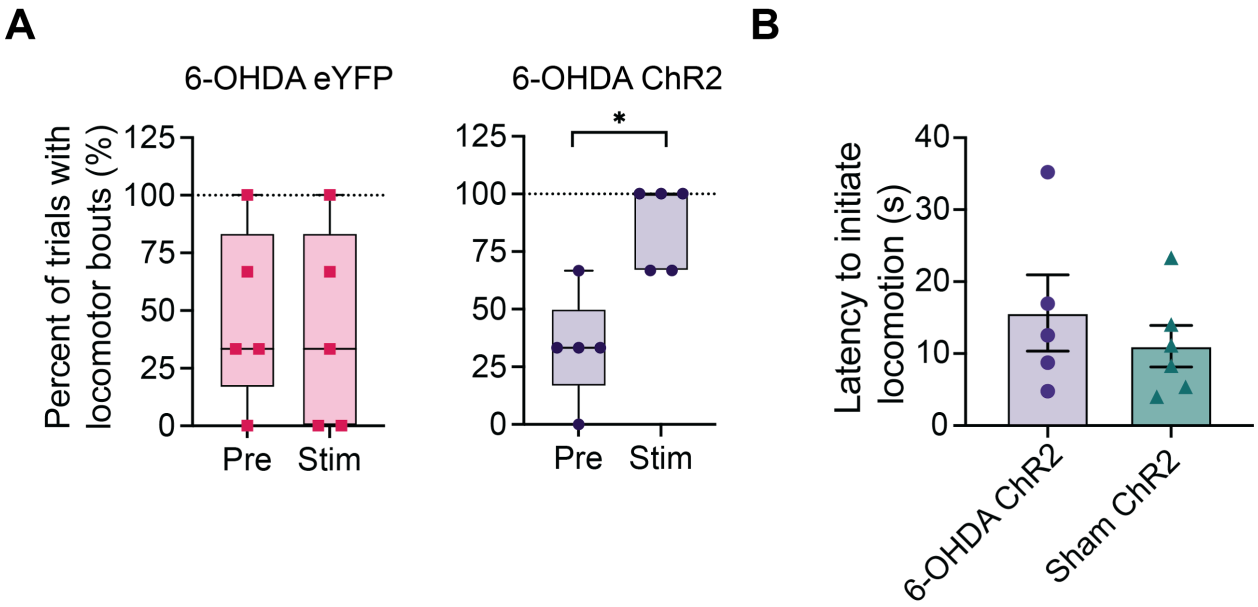

Figure 3 - figure supplement 2. Characterization of A13 region photoactivation temporal dynamics on locomotion initiation. (A) Percentage of trials in which at least one bout of locomotion was observed. Data are plotted as box-and-whisker plots, with the horizontal line within the box indicating the group median, the interquartile range represented by the box edges, and the whiskers denoting group minimum and maximum. Asterisks indicate significant comparisons using the Wilcoxon signed-rank test: *$p = 0.71$. **(B)** The average latency to initiate locomotion after photoactivation onset in ChR2-group animals was not significantly different from that of sham controls ($p = 0.953$). Means are plotted with error bars indicating ± SEM.

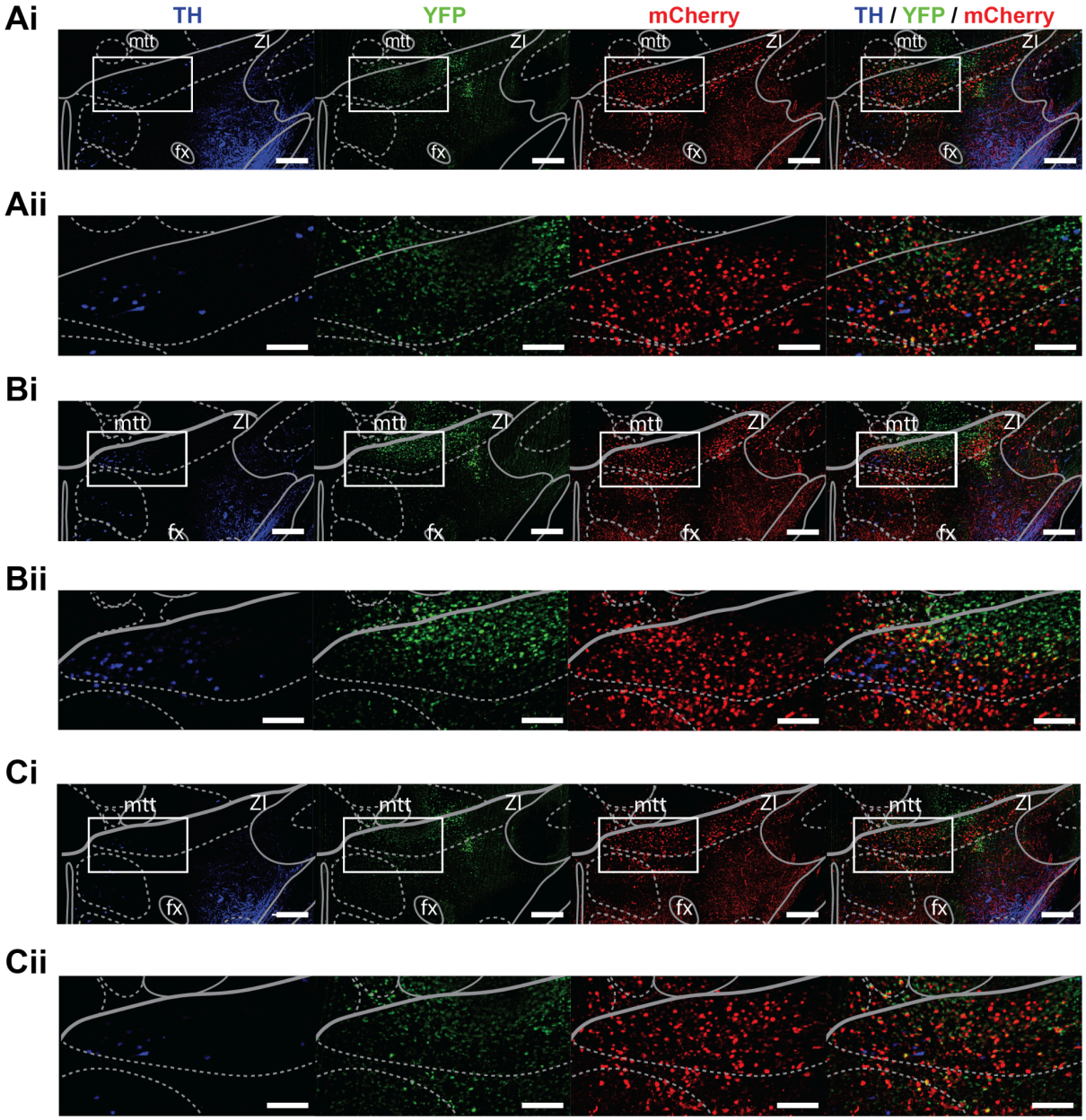

Figure 4 - figure supplement 1. **Injection core in a sham brain showing viral tracer spread in the A13 region.** Viral tracers (AAV8-CamKII-mCherry and AAVrg-CAG-GFP) were mixed 1:1. Light-sheet images around the injection site were acquired using a 2x objective, 6.3x optical zoom, and a z-step size of 2 µm (xyz resolution = 0.477 µm x 0.477 µm x 2 µm). Background filtering (median value of 20 pixels and Gaussian smoothing with a sigma value of 10) was performed in ImageJ software and visualized in IMARIS 9.8 (Belfast, United Kingdom). Images from the 2008 Allen Reference Atlas were overlaid on 90 µm maximum intensity projections taken from IMARIS 9.8 (Belfast, United Kingdom): -1.26 mm **(A)**, -1.36 mm **(B)**, and -1.46 mm **(C)**. Zoomed-in sections of each white rectangular region at each coordinate (rows '**i**') are displayed below for each fluorophore (rows '**ii**'). Scale bars: 200 µm for rows 'i' and 100 µm for rows 'ii'.

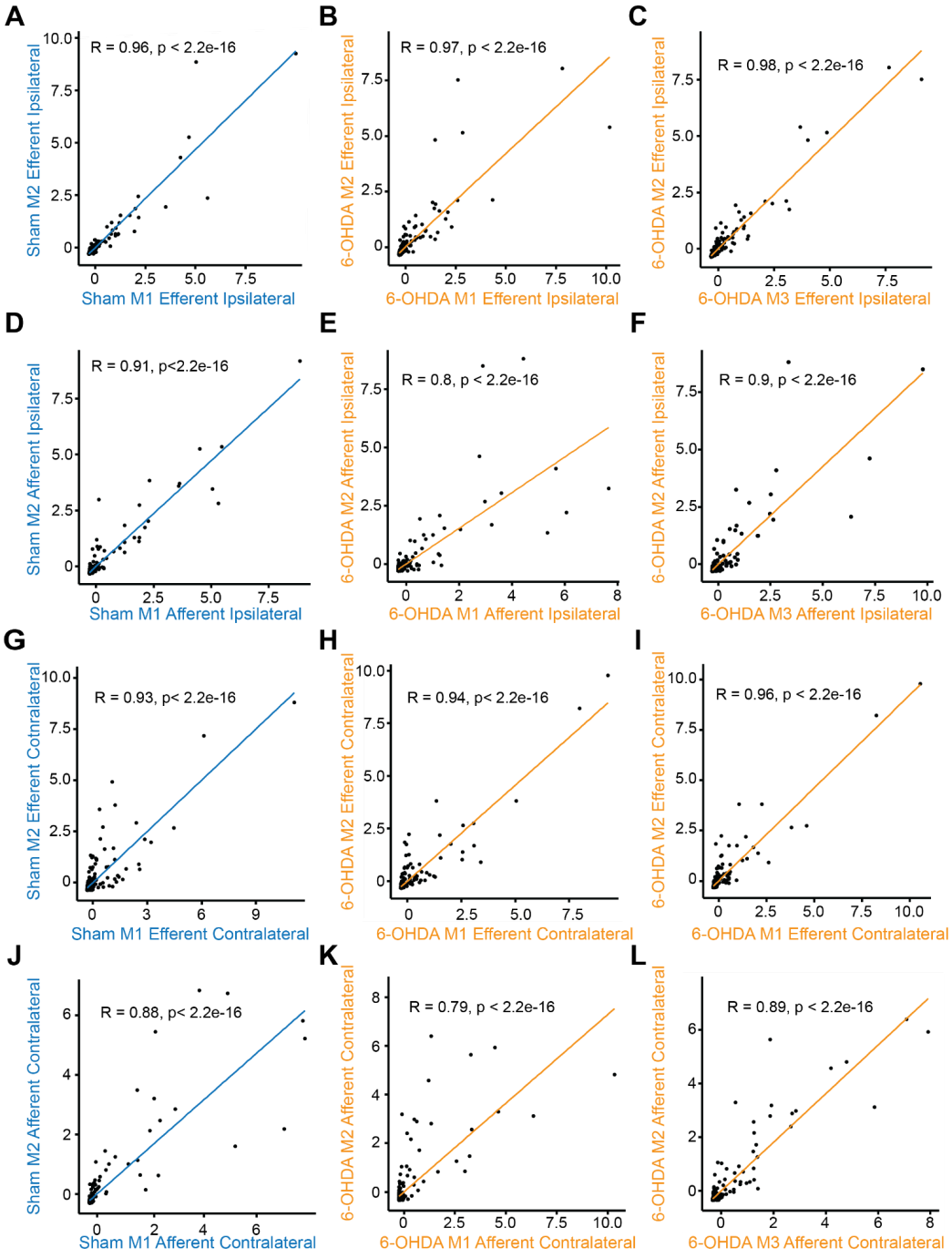

Figure 5 – figure supplement 1. Ipsilateral (A–F) and contralateral (G–L) afferent and efferent proportions in sham (blue) and 6-OHDA (orange) mice. An experimental variation on the total labeling of neurons and fibers was minimized by dividing the afferent cell counts or efferent fiber areas in each brain region by the total number found in a brain to obtain the proportion of total inputs and outputs. Using Spearman's correlation analysis, we found afferent and efferent proportions across animals to be consistent among each other with an average correlation of 0.91 (SEM = 0.02). M1 = mouse #1, M2 = mouse #2, M3 = mouse #3.

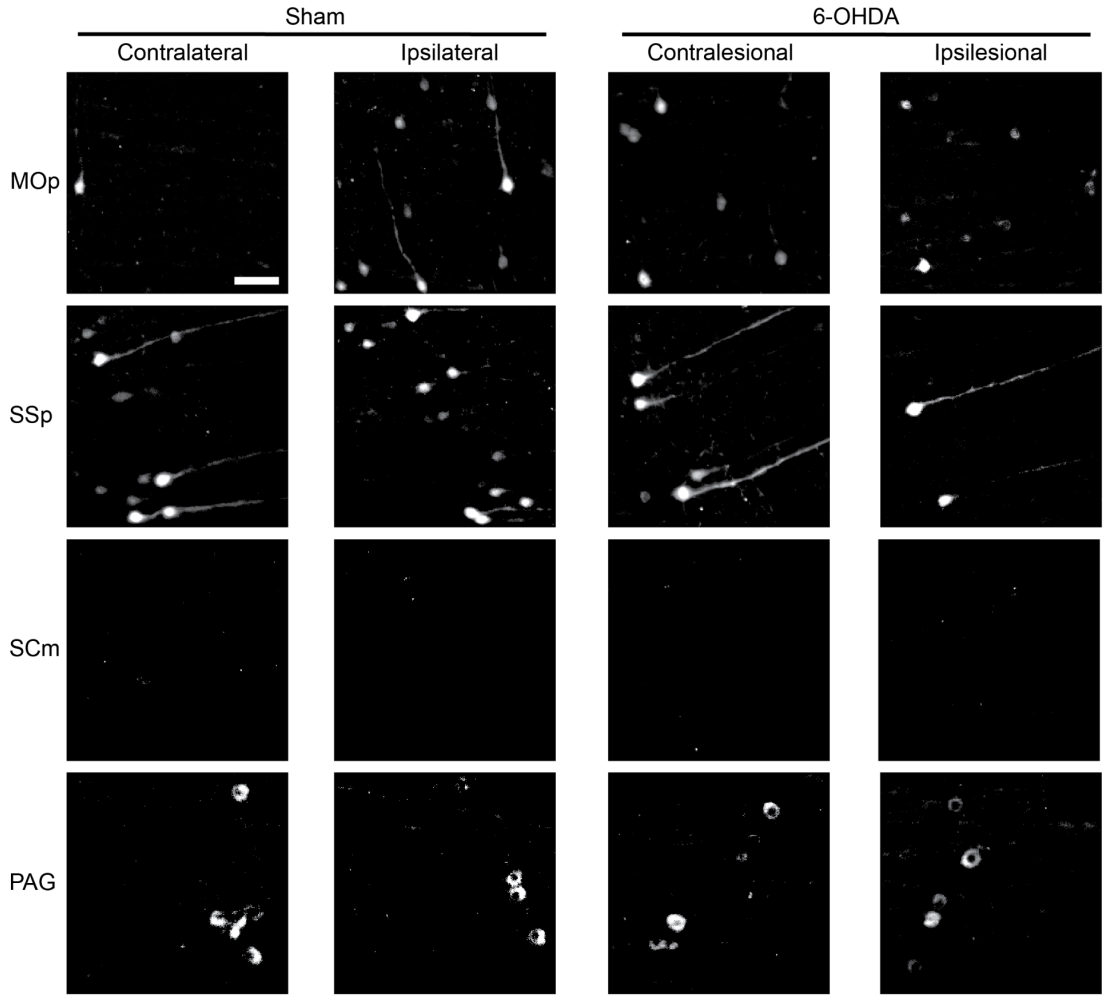

Figure 6 – figure supplement 1. Examples of retrogradely labeled GFP-positive fibers and cells from selected regions illustrating projections to the A13 region. Cell bodies projecting to A13 were visualized through whole-brain imaging. GFP expression was detected using light-sheet microscopy with a 2× objective, 6.3× optical zoom, and a z-step size of 2 µm (xyz resolution: 0.477 µm × 0.477 µm × 2 µm). Brain regions were delimited by registration with the Allen Brain Atlas (see Methods) and cropped from selected 90 µm image stacks using ImageJ software. A background filter (Gaussian smoothing with a rolling ball radius of 20 pixels) and a minimum filter (radius = 1 pixel) were applied in ImageJ. Scale bar = 50 µm.

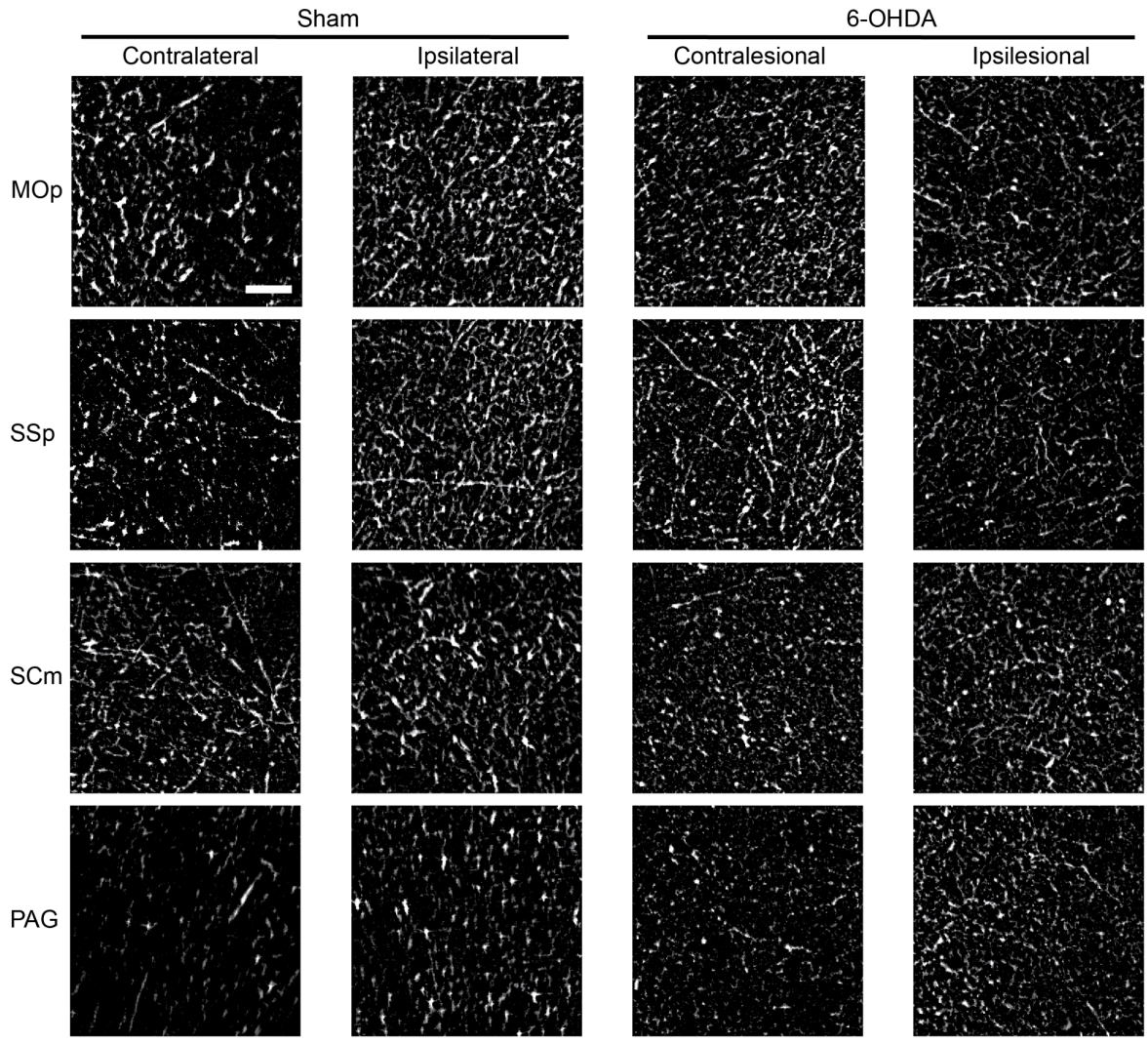

Figure 6 – figure supplement 2. Examples of anterogradely labeled mCherry-positive fibers from selected regions illustrating projections to the A13 region. mCherry expression was detected using light-sheet microscopy with a 2× objective, 6.3× optical zoom, and a z-step size of 2 µm (xyz resolution: 0.477 µm × 0.477 µm × 2 µm). Brain regions were delineated by registration with the Allen Brain Atlas (see Methods) and cropped from selected 90 µm image stacks using ImageJ software. A background filter (Gaussian smoothing with a rolling ball radius of 5 pixels) and a minimum filter (radius = 1 pixel) were applied in ImageJ. Scale bar = 50 µm.

Figure 3—Video S1

Photoactivation of the A13 region in a 6-OHDA model mouse producing increased locomotion in the OFT (2x speed).

Figure 3—Video S2

Photoactivation of the A13 region in a sham mouse producing increased locomotion in the OFT (2x speed).

Figure 3—Video S3

Photoactivation of the A13 region during the pole test in a 6-OHDA model mouse decreases pole descent time (0.5x speed).